# Can Training Dynamics of Scale-Invariant Neural Networks Be Explained by the Thermodynamics of an Ideal Gas?

## Ildus Sadrtdinov<sup>1</sup>, Ekaterina Lobacheva<sup>2,3</sup>, Ivan Klimov<sup>1</sup>, Mikhail I. Katsnelson<sup>1,4</sup>, Dmitry Vetrov<sup>1</sup>

<sup>1</sup>Constructor University <sup>2</sup>Mila – Quebec AI Institute, <sup>3</sup>Université de Montréal <sup>4</sup>Institute for Molecules and Materials, Radboud University, NL-6525 AJ Nijmegen, The Netherlands Correspondence: isadrtdinov@constructor.university

#### Abstract

Understanding the training dynamics of deep neural networks remains a major open problem, with physics-inspired approaches offering promising insights. Building on this perspective, we develop a thermodynamic framework to describe the stationary distributions of stochastic gradient descent (SGD) with weight decay for scale-invariant neural networks, a setting that both reflects practical architectures with normalization layers and permits theoretical analysis. We establish analogies between training hyperparameters (e.g., learning rate, weight decay) and thermodynamic variables such as temperature, pressure, and volume. Starting with a simplified isotropic noise model, we uncover a close correspondence between SGD dynamics and ideal gas behavior, validated through theory and simulation. Extending to training of neural networks, we show that key predictions of the framework, including the behavior of stationary entropy, align closely with experimental observations. This framework provides a principled foundation for interpreting training dynamics and may guide future work on hyperparameter tuning and the design of learning rate schedulers.

#### 1 Introduction

The machine learning community has long noted that, despite the strong performance of deep neural networks, their optimization dynamics remain poorly understood. A promising way to address this challenge is to draw inspiration from physics, which also studies systems with many degrees of freedom and complex interactions. Among these, thermodynamics has been especially influential, with numerous works connecting it to neural networks (Jastrzebski et al., 2017;

Chen et al., 2024; Zhang, 2024; Kozyrev, 2025). In this work, we extend this line of research and propose a framework that relates neural network optimization to thermodynamic systems. Specifically, we interpret stochastic gradient noise as thermal fluctuations and introduce macroscopic thermodynamic variables, like temperature, pressure, and volume, to describe stationary distributions of stochastic gradient descent (SGD). We also connect these variables to training hyperparameters such as learning rate and weight decay.

We focus on *scale-invariant* neural networks, which resemble common architectures with normalization layers (e.g., BatchNorm (Ioffe and Szegedy, 2015), Layer-Norm (Ba et al., 2016)), while remaining amenable to rigorous theoretical analysis. Previous studies largely overlooked the role of scale invariance and primarily explored thermodynamic analogies involving energy, entropy, and temperature. In contrast, we show that the optimization of scale-invariant networks under SGD with weight decay naturally extends this framework to include well-defined notions of pressure and volume, establishing a direct correspondence with the ideal gas law. Our main contributions are:

- We propose a framework linking thermodynamics to optimization of scale-invariant functions. The analogy is grounded in stationary SGD distributions derived from Stochastic Differential Equations (SDEs).
- 2. We analyze three training protocols: (1) fixed parameter norm, (2) fixed effective learning rate (ELR), and (3) fixed learning rate (LR); derive the corresponding SDEs, and map them to thermodynamic processes.
- 3. Using a simplified *isotropic noise model*, we prove the thermodynamic analogy rigorously and confirm it with simulations. Interestingly, the model closely mirrors the behavior of an ideal gas, one of the simplest thermodynamic systems.

4. We discuss how the ideal gas model generalizes to actual training of scale-invariant neural networks. Our framework accurately predicts, how the entropy of the stationary distribution changes, when varying learning rate and weight decay.

Overall, our framework reveals a deep link between optimization and thermodynamics, providing a physics-based foundation for interpreting neural network training. This insight can inform future work on training hyperparameters, including learning rate scheduling.

#### 2 Background

In this section, we outline the main concepts from thermodynamics and the optimization of scale-invariant neural networks that form the basis of our analogy. For convenience, a complete list of notations is provided in Appendix A. A broader overview of related work is given in Appendix B.

**Thermodynamics** Below we summarize the key principles of thermodynamics relevant to our discussion. A more detailed introduction is given in Appendix C.

- **T1** A thermodynamic system is described by state variables, including internal energy U (the total energy of all particles in the system), entropy S (a measure of disorder), temperature T, pressure p, and volume V.
- **T2** The First Law of Thermodynamics expresses energy conservation:  $\mathrm{d}U = \delta Q p\,\mathrm{d}V$ , where  $\delta Q$  is the infinitesimal heat supplied to the system. The Second Law of Thermodynamics requires  $\mathrm{d}S \geq \delta Q/T$ , implying that systems evolve toward equilibrium, where an appropriate thermodynamic potential is minimized (**T4**, **T5**). A reversible process satisfies  $\mathrm{d}S = \delta Q/T$ .
- **T3** The Gibbs distribution connects thermodynamics with statistical mechanics. At equilibrium, the probability of microstate i with energy  $E_i$  is  $p_i \propto \exp(-E_i/T)$ , with the temperature T controlling the distribution's spread. Internal energy and entropy can be expressed as  $U = \mathbb{E}_{p_i}[E_i]$  and  $S = \mathbb{E}_{p_i}[-\log p_i]$ .
- **T4** At fixed T and V, the Helmholtz energy F = U TS is minimized at equilibrium. The Maxwell relation links derivatives of state variables and helps to determine changes in entropy, which is otherwise difficult to measure. In this case, it is

given by 
$$\left(\frac{\partial S}{\partial V}\right)_T = \left(\frac{\partial p}{\partial T}\right)_V^{-1}$$
.

- **T5** At fixed T and p, the Gibbs energy G = U TS + pV is minimized at equilibrium, with Maxwell relation  $-\left(\frac{\partial S}{\partial p}\right)_T = \left(\frac{\partial V}{\partial T}\right)_p$ .
- **T6** An *ideal gas* is a simplified model neglecting intermolecular interactions. At equilibrium, its state variables satisfy the *ideal gas law* pV = RT, where R is the gas constant.
- **T7** The isochoric and isobaric heat capacities are  $C_V = \left(\frac{\delta Q}{\mathrm{d}T}\right)_V$  and  $C_p = \left(\frac{\delta Q}{\mathrm{d}T}\right)_p$ . For an ideal gas, both are constants with  $C_p C_V = R$ . In an adiabatic process, defined by  $\delta Q = 0$ , the ideal gas follows  $pV^{\gamma} = \mathrm{const}$  with  $\gamma = C_p/C_V$ .

Stationary behavior of SGD In classical optimization theory, SGD differs from full-batch gradient descent: instead of converging to a single stationary point of the loss function, SGD converges to a stationary distribution centered around it. We denote this distribution by  $\rho_{\boldsymbol{w}}(\boldsymbol{w})$ , where  $\boldsymbol{w} \in \mathbb{R}^d$  are the model parameters. This behavior arises from two factors: (1) the finite learning rate and (2) the stochastic gradient estimates. Both inject noise into the optimization process, analogous to thermal fluctuations, making thermodynamics a natural framework for analysis.

Scale-invariant neural networks Modern architectures often include normalization layers that make preceding parameters scale-invariant, i.e., the output of the normalization layer is independent of the parameter norm. We focus on fully scale-invariant networks, where the whole output of the network does not depend on the parameter norm (i.e., only on the unit direction vector of the weights). Accordingly, the loss function satisfies  $L(\alpha w) = L(w)$  for all  $\alpha > 0$ . Gradients of scale-invariant functions obey: (P1)  $\nabla L(\alpha w) = \frac{1}{\alpha} \nabla L(w)$  and (P2)  $w^T \nabla L(w) = 0$ (see Lemma 3.1 of Li et al. (2020)). These hold for both full-batch and stochastic gradients. The dynamics of the model on the unit sphere (i.e., the loss evolution) is governed by the effective learning rate (ELR), defined as  $\eta_{\text{eff}} = \eta/\|\boldsymbol{w}\|^2$ , where  $\eta$  is the usual learning rate (LR) used in SGD iterates.

#### 3 Thermodynamic framework

#### 3.1 Thermodynamic analogy

In this section, we introduce optimization quantities that correspond to the thermodynamic state variables

Here,  $\left(\frac{\partial f}{\partial x}\right)_y$  denotes the partial derivative of f w.r.t. x while keeping y constant.

in **T1**. Lowering the LR value or the gradient noise variance (e.g., by increasing batch size) makes the stationary distribution of SGD concentrate closer to a loss minimum. This mirrors the role of temperature T in the Gibbs distribution (**T3**): as  $T \to 0$ , the system minimizes internal energy U by occupying the lowest-energy state  $E_i$ , just as full-batch gradient descent converges to the loss minimum. This motivates the identifications  $i \leftrightarrow \boldsymbol{w}$ ,  $E_i \leftrightarrow L(\boldsymbol{w})$ , and  $U \leftrightarrow \mathbb{E}_{\rho_{\boldsymbol{w}}}[L(\boldsymbol{w})]$ . A precise definition of T will be given in Section 3.2, but we already hypothesize that it depends on both the learning rate and gradient noise variance.

For scale-invariant networks, training dynamics naturally splits into the parameter radius  $r = \|\boldsymbol{w}\|$  and the unit direction vector  $\overline{\boldsymbol{w}} = \boldsymbol{w}/r$  (Li et al., 2020; Wan et al., 2021). Theoretic results based on SDE (reviewed in Section 3.2) show that r evolves deterministically and converges to a constant  $r^*$ . Thus, the stationary weight distribution factorizes as  $\rho_{\boldsymbol{w}}(\boldsymbol{w}) = \rho_{\overline{\boldsymbol{w}}}(\overline{\boldsymbol{w}})\,\delta(r-r^*)$ , where  $\delta$  is the Dirac delta. The internal energy becomes  $U = \mathbb{E}_{\rho_{\boldsymbol{w}}}[L(\boldsymbol{w})] = \mathbb{E}_{\rho_{\overline{\boldsymbol{w}}}}[L(\overline{\boldsymbol{w}})]$ . We define the entropy of the stationary distribution as

$$S(\rho_{\mathbf{w}}) = S(\rho_{\overline{\mathbf{w}}}) + (d-1)\log r^*, \tag{1}$$

where  $S(\rho_{\overline{w}}) = \mathbb{E}_{\rho_{\overline{w}}}[-\log \rho_{\overline{w}}(\overline{w})]$ . The first term measures entropy on the unit sphere, while the second term accounts for stretching the distribution  $\rho_{\overline{w}}$  to the sphere of radius  $r^*$ .

Finally, we assign analogues of pressure and volume:  $p \leftrightarrow \lambda$ , the weight decay (WD) coefficient, and  $V \leftrightarrow \frac{r^2}{2}$ . Here  $r^2$  captures how widely weights spread in parameter space ("volume"), while  $\lambda$  controls the strength of weight decay pulling weights toward the origin ("pressure"). Notably, the pV term in the Gibbs energy G = U - TS + pV (T5) directly parallels the L2 regularization term  $\lambda \frac{r^2}{2}$ . This correspondence will be established rigorously in the next section.

#### 3.2 From SDE to thermodynamics

In this section, we begin with a stochastic differential equation (SDE) established in prior work (Li et al., 2020; Wang and Wang, 2022), which captures the general training dynamics of scale-invariant neural networks. We then introduce the *isotropic noise model* and show that its SDE solutions lead to a self-consistent thermodynamic description of stationary distributions of SGD. We consider three training protocols of increasing complexity. Formal proofs are deferred to Appendix D, and we revisit the case of neural networks in Section 6.

SGD on a fixed sphere A natural approach to handling scale-invariant parameters is to optimize

them directly on their intrinsic domain, a sphere of fixed radius. This can be implemented by projecting weights back to the sphere after each iteration (Kodryan et al., 2022; Loshchilov et al., 2025) or via Riemannian optimization techniques (Cho and Lee, 2017). Here we focus on projected SGD on a sphere  $\mathbb{S}^{d-1}(r)$  of radius r, with discrete dynamics

$$\mathbf{w}_{k+1} = \operatorname{proj}_{\mathbb{S}^{d-1}(r)} (\mathbf{w}_k - \eta \nabla L_{\mathcal{B}_k}(\mathbf{w}_k)),$$
 (2)

where  $L_{\mathcal{B}_k}(\boldsymbol{w}_k)$  denotes the loss for a mini-batch of data  $\mathcal{B}_k$ . Note that weight decay is absent here, since the norm of  $\boldsymbol{w}$  is fixed by construction.

Following Jastrzębski et al. (2017); Mandt et al. (2017), we approximate noise in stochastic gradients with a Gaussian random vector

$$\nabla L_{\mathcal{B}_k}(\boldsymbol{w}) \approx \nabla L(\boldsymbol{w}) + (\boldsymbol{\Sigma}_{\boldsymbol{w}})^{1/2} \boldsymbol{\varepsilon},$$
 (3)

where  $\varepsilon \sim \mathcal{N}(0, \mathbf{I}_d)$  and  $\Sigma_{\boldsymbol{w}}$  is a spatially dependent covariance matrix of stochastic gradients<sup>2</sup>. Due to properties (P1) and (P2), the following relations hold:

$$\nabla L(\boldsymbol{w}) = \nabla L(\overline{\boldsymbol{w}})/r \qquad \boldsymbol{w}^T \nabla L(\boldsymbol{w}) = 0$$
 (4)

$$\Sigma_{\boldsymbol{w}} = \Sigma_{\overline{\boldsymbol{w}}}/r^2 \qquad (\Sigma_{\boldsymbol{w}})^{1/2} \boldsymbol{w} = 0$$
 (5)

Taking the continuous-time limit of Eq. 2, we obtain the SDE for the direction vector  $\overline{\boldsymbol{W}}_t$ 

$$d\overline{\boldsymbol{W}}_{t} = -\left[\eta_{\text{eff}}\nabla L(\overline{\boldsymbol{W}}_{t}) + \frac{\eta_{\text{eff}}^{2}}{2}\operatorname{Tr}\left(\boldsymbol{\Sigma}_{\overline{\boldsymbol{W}}_{t}}\right)\overline{\boldsymbol{W}}_{t}\right]dt + \eta_{\text{eff}}\left(\boldsymbol{\Sigma}_{\overline{\boldsymbol{W}}_{t}}\right)^{\frac{1}{2}}d\boldsymbol{B}_{t},$$

$$(6)$$

where  $\boldsymbol{B}_t$  denotes standard Brownian motion in  $\mathbb{R}^d$  and  $\eta_{\text{eff}} = \eta/r^2$  is the ELR. While Wang and Wang (2022) analyze the Riemannian version of this SDE, we remain with the Euclidean formulation.

A common simplifying assumption for further analysis is the **isotropic noise model**, where the covariance matrix is

$$\Sigma_{\overline{W}_t} = P_{\overline{W}_t} \Sigma P_{\overline{W}_t}, \ P_{\overline{W}_t} = I_d - \overline{W}_t \overline{W}_t^T, \ \Sigma = \sigma^2 I_d,$$

with  $P_{\overline{W}_t}$  projecting onto the tangent subspace orthogonal to  $\overline{W}_t$ , ensuring the constraints of Eq. 5, and  $\sigma$  is a positive scalar. Under this assumption, the stationary distribution can be found analytically

$$\rho_{\overline{w}}^*(\overline{w}) \propto \exp\left(-\frac{L(\overline{w})}{\tau_{\text{eff}}}\right),$$
(7)

with  $\tau_{\rm eff} = \frac{\eta_{\rm eff} \sigma^2}{2}$ . This is exactly the Gibbs distribution (**T3**), with energy  $E_i = L(\overline{\boldsymbol{w}})$  and temperature

 $<sup>^2 \</sup>text{We}$  make  $\Sigma_{\overline{w}}$  implicitly dependent on batch size and thus do not consider the batch size explicitly.

 $T = \tau_{\text{eff}}$ . It is also well known that this distribution minimizes the Helmholtz free energy F = U - TS (**T4**) among all possible distributions Le Ny (2008).

In the isotropic noise model, SGD with fixed ELR  $\eta_{\text{eff}}$  on a sphere minimizes the Helmholtz energy F = U - TS with  $T = \frac{\eta_{\text{eff}} \sigma^2}{2}$ .

SGD with fixed ELR We now allow the radius to evolve and explicitly introduce weight decay into the dynamics. We consider training with a fixed ELR, which ensures that the dynamics of the loss remain independent of the parameter norm. This is implemented by scaling the learning rate with the squared norm of the current parameters,  $\eta = \eta_{\text{eff}} ||\boldsymbol{w}_k||^2$ . Although less common, such ELR control is occasionally used in practice (Lyle et al., 2024; Ali Mehmeti-Göpel and Wand, 2024), e.g., for enhancing plasticity in reinforcement learning. The discrete update rule is

$$\boldsymbol{w}_{k+1} = \boldsymbol{w}_k - \eta_{\text{eff}} \|\boldsymbol{w}_k\|^2 \Big( \nabla L_{\mathcal{B}_k}(\boldsymbol{w}_k) + \lambda \boldsymbol{w}_k \Big)$$
 (8)

The corresponding SDE takes the form

$$d\mathbf{W}_{t} = -\eta_{\text{eff}} \|\mathbf{W}_{t}\|^{2} \left(\nabla L(\mathbf{W}_{t}) + \lambda \mathbf{W}_{t}\right) dt +$$

$$+ \eta_{\text{eff}} \|\mathbf{W}_{t}\|^{2} \left(\mathbf{\Sigma}_{\mathbf{W}_{t}}\right)^{\frac{1}{2}} d\mathbf{B}_{t}$$
(9)

Applying Ito's formula yields separate dynamics for the direction vector  $\overline{\boldsymbol{W}}_t$  and the radius  $r_t$ :

$$d\overline{\boldsymbol{W}}_{t} = -\left[\eta_{\text{eff}}\nabla L(\overline{\boldsymbol{W}}_{t}) + \frac{\eta_{\text{eff}}^{2}}{2}\operatorname{Tr}\left(\boldsymbol{\Sigma}_{\overline{\boldsymbol{W}}_{t}}\right)\overline{\boldsymbol{W}}_{t}\right]dt + + \eta_{\text{eff}}\left(\boldsymbol{\Sigma}_{\overline{\boldsymbol{W}}_{t}}\right)^{\frac{1}{2}}d\boldsymbol{B}_{t}$$

$$(10)$$

$$\frac{\mathrm{d}r_t}{\mathrm{d}t} = -\eta_{\text{eff}} \lambda r_t^3 + \frac{\eta_{\text{eff}}^2}{2} r_t \operatorname{Tr} \mathbf{\Sigma}_{\overline{\mathbf{W}}_t}$$
 (11)

The radius indeed evolves deterministically.

Under the **isotropic noise assumption**, the stationary radius is

$$r^* = \sqrt{\frac{\eta_{\text{eff}}\sigma^2(d-1)}{2\lambda}} = \sqrt{\frac{\tau_{\text{eff}}(d-1)}{\lambda}}$$
 (12)

Meanwhile, the dynamics of  $\overline{W}_t$  remain identical to the fixed-sphere case, so the stationary distribution  $\rho_{\overline{w}}$  is still given by Eq. 7 with temperature  $T = \tau_{\text{eff}}$ . If we identify pressure as  $p = \lambda$ , then the stationary radius satisfies the ideal gas law (**T6**) with R = (d-1)/2

$$V = \frac{(r^*)^2}{2} = \frac{\tau_{\text{eff}}(d-1)}{2\lambda} = \frac{RT}{r}$$
 (13)

Moreover, we can show that this value of V minimizes the Gibbs energy G (T5). The Gibbs energy decomposes into two terms, one depending only on  $\rho_{\overline{w}}$  and

the other only on V:

$$G = U(\rho_{\mathbf{w}}) - TS(\rho_{\mathbf{w}}) + pV =$$

$$= \underbrace{U(\rho_{\overline{\mathbf{w}}}) - TS(\rho_{\overline{\mathbf{w}}})}_{\text{depends on } \rho_{\overline{\mathbf{w}}}} - \underbrace{\frac{T(d-1)}{2}\log(2V) + pV}_{\text{depends on } V}$$
(14)

The first term is minimized because  $\rho_{\overline{w}}$  is the Gibbs distribution with temperature T, while the second is minimized at  $V = \frac{T(d-1)}{2p}$ .

In the isotropic noise model, SGD with fixed ELR  $\eta_{\text{eff}}$  and WD  $\lambda$  minimizes Gibbs energy G = U - TS + pV with  $T = \frac{\eta_{\text{eff}} \sigma^2}{2}$  and  $p = \lambda$ .

SGD with fixed LR. We now turn to the case of training with a fixed LR. Here, the dynamics on the unit sphere explicitly depends on the parameter norm. An SGD update takes the form

$$\boldsymbol{w}_{k+1} = \boldsymbol{w}_k - \eta \Big( \nabla L_{\mathcal{B}_k}(\boldsymbol{w}_k) + \lambda \boldsymbol{w}_k \Big), \qquad (15)$$

which corresponds to the SDE

$$d\mathbf{W}_{t} = -\eta \left( \nabla L(\mathbf{W}_{t}) + \lambda \mathbf{W}_{t} \right) dt + \eta \left( \mathbf{\Sigma}_{\mathbf{W}_{t}} \right)^{\frac{1}{2}} d\mathbf{B}_{t}$$
 (16)

The induced dynamics for the direction  $\overline{\boldsymbol{W}}_t$  and the radius  $r_t$  are

$$d\overline{\boldsymbol{W}}_{t} = -\left[\frac{\eta}{r_{t}^{2}}\nabla L(\overline{\boldsymbol{W}}_{t}) + \frac{\eta^{2}}{2r_{t}^{4}}\left(\operatorname{Tr}\boldsymbol{\Sigma}_{\overline{\boldsymbol{W}}_{t}}\right)\overline{\boldsymbol{W}}_{t}\right]dt + + \frac{\eta}{r_{t}^{2}}\left(\boldsymbol{\Sigma}_{\overline{\boldsymbol{W}}_{t}}\right)^{\frac{1}{2}}d\boldsymbol{B}_{t}$$
(17)

$$\frac{\mathrm{d}r_t}{\mathrm{d}t} = -\eta \lambda r_t + \frac{\eta^2}{2r_t^3} \operatorname{Tr} \mathbf{\Sigma}_{\overline{W}_t}$$
 (18)

Under the **isotropic noise model**, let  $\tau = \frac{\eta \sigma^2}{2}$ . The stationary radius and angular distribution are then

$$r^* = \sqrt[4]{\frac{\tau(d-1)}{\lambda}}, \quad \rho_{\overline{\boldsymbol{w}}}^*(\overline{\boldsymbol{w}}) \propto \exp\left(-\frac{L(\overline{\boldsymbol{w}})}{\tau/(r^*)^2}\right)$$
 (19)

This is again a Gibbs distribution with temperature

$$T = \frac{\tau}{(r^*)^2} = \sqrt{\frac{\tau\lambda}{d-1}} = \sqrt{\frac{\eta\lambda\sigma^2}{2(d-1)}}$$
 (20)

The stationary radius also satisfies the ideal gas law

$$V = \frac{(r^*)^2}{2} = \frac{1}{2} \sqrt{\frac{\tau(d-1)}{\lambda}} = \frac{RT}{p},$$
 (21)

with R=(d-1)/2 and  $p=\lambda$ . Thus, the stationary distribution derived from the SDE minimizes the Gibbs energy G.

In the isotropic noise model, SGD with fixed LR  $\eta$  and WD  $\lambda$  minimizes the Gibbs energy G=U-TS+pV with  $T=\sqrt{\frac{\eta\lambda\sigma^2}{2(d-1)}}$  and  $p=\lambda$ .

#### 4 Empirical validation

To support our theoretical framework, we design a set of experiments derived from the thermodynamic analogy. We focus on tests that cannot be directly deduced from the SDE formulation, making them strong evidence for the thermodynamic perspective.

(V1) Stationary radius The SDE predicts that the stationary radius scales as  $\sqrt[4]{\eta/\lambda}$  when training with a fixed LR, and as  $\sqrt{\eta_{\rm eff}/\lambda}$  when training with a fixed ELR. Since this prediction follows directly from the SDE (without invoking thermodynamics), it primarily serves as a sanity check. At the same time, it also verifies the ideal gas law (T6) in our analogy.

(V2) Minimizing thermodynamic potentials Our analogy predicts that stationary SGD dynamics minimize the appropriate thermodynamic potential: Helmholtz energy F (T4) or Gibbs energy G (T5), depending on the training protocol. Of course, numerical experiments cannot test minimization over the entire space of distributions  $\rho_{\overline{w}}$  and radii  $r^*$ . Instead, we check whether the observed stationary states minimize F or G at least among the distributions induced by different hyperparameter settings.

For example, in fixed LR training, consider a set of hyperparameter configurations  $S = \{(\eta_i, \lambda_i)\}_{i=1}^S$ . For each  $(\eta_i, \lambda_i)$ , we train the model and measure the corresponding energy  $U_i$ , entropy  $S_i$ , and volume  $V_i$ . We then verify that for each  $(\eta^*, \lambda^*) \in S$ :

$$(\eta^*, \lambda^*) = \underset{(\eta_i, \lambda_i) \in \mathcal{S}}{\operatorname{argmin}} \left\{ U_i - T^* S_i + p^* V_i \right\}, \qquad (22)$$

where  $T^* = \sqrt{\frac{\eta^*\lambda^*\sigma^2}{2(d-1)}}$  and  $p^* = \lambda^*$ . A similar procedure applies for the settings with a fixed ELR or on a fixed sphere.

(V3) Maxwell relations Maxwell relations describe how entropy S varies when thermodynamic variables change (T4, T5). In our setting, training with fixed LR corresponds to fixing p and T, so the relevant Maxwell relation is  $\left(\frac{\partial S}{\partial p}\right)_T = \left(\frac{\partial V}{\partial T}\right)_p$ . In Appendix D.3, we show this can be equivalently written as

$$\left(\frac{\partial S}{\partial \log \eta}\right)_{\lambda} - \left(\frac{\partial S}{\partial \log \lambda}\right)_{\eta} = \frac{d-1}{2} \tag{23}$$

This elegant equation quantifies, how the two hyperparameters influence the stationary entropy. Analogous relations for the fixed sphere and fixed ELR training protocols are also derived there.

(V4) Adiabatic process Previously, we viewed convergence to a stationary distribution as a nonreversible thermodynamic process. Here, however, we reinterpret stationary distributions induced by different hyperparameters as states of a reversible process. This perspective allows us to analyze how hyperparameters shape the stationary distribution through our thermodynamic lens. In particular, we focus on the adiabatic process, characterized by  $\delta Q = 0$  (T7). Although heat Q does not appear explicitly in our analogy, we can infer it from the First Law (**T2**):  $\delta Q =$ dU + pdV. This allows us to compute the isochoric  $C_V$ and isobaric  $C_p$  heat capacities, defined in **T7**. In Appendix D.4, we show that  $C_p - C_V = \frac{d-1}{2} = R$ , exactly as in the ideal gas model. To simulate an adiabatic process, we vary  $(\eta, \lambda)$  jointly such that  $pV^{\gamma} = \text{const}$ with  $\gamma = C_p/C_V$ . Since  $dS = \delta Q/T = 0$  for a reversible process (T2), entropy S should remain constant. Empirically, this means that the stationary distributions observed on spheres of different radii should have identical entropy. The adiabatic process provides a way to explore how changing hyperparameters can reshape the weight distribution without altering its overall "disorder".

#### 5 Isotropic noise model experiments

**Experimental setup** We start by validating the isotropic noise model through numerical simulation. Here, we show results for fixed LR, while other training protocols are presented in Appendix E. We consider a scale-invariant function  $L(\boldsymbol{w}) = 1 + \frac{\boldsymbol{\mu}^T \boldsymbol{w}}{\|\boldsymbol{w}\|}$  with some fixed  $\boldsymbol{\mu} \in \mathbb{R}^d$ ,  $\|\boldsymbol{\mu}\| = 1$  and train it using noisy gradient descent:

$$\boldsymbol{w}_{k+1} = \boldsymbol{w}_k - \eta \Big( \nabla L(\boldsymbol{w}_k) + \frac{1}{\|\boldsymbol{w}_k\|} \boldsymbol{P}_{\overline{\boldsymbol{w}}_k} \sigma \boldsymbol{\varepsilon} + \lambda \boldsymbol{w}_k \Big), (24)$$

with  $\varepsilon \sim \mathcal{N}(0, \mathbf{I}_d)$ . We select this function because the SDE theory predicts that, at stationarity, the angular distribution follows a Von Mises-Fisher (VMF) form:  $\rho_{\overline{w}}(\overline{w}) \propto \exp(-\mu^T \overline{w}/T)$ . For this distribution, the analytical values of U and S are known (see Appendix E), allowing direct comparison with simulation results. In this setting, we set d=3.

Entropy estimation While calculating mean training loss U is straightforward, estimating entropy S is a more complicated task. We rely on the nearest neighbor entropy estimator (Kozachenko and Leonenko,

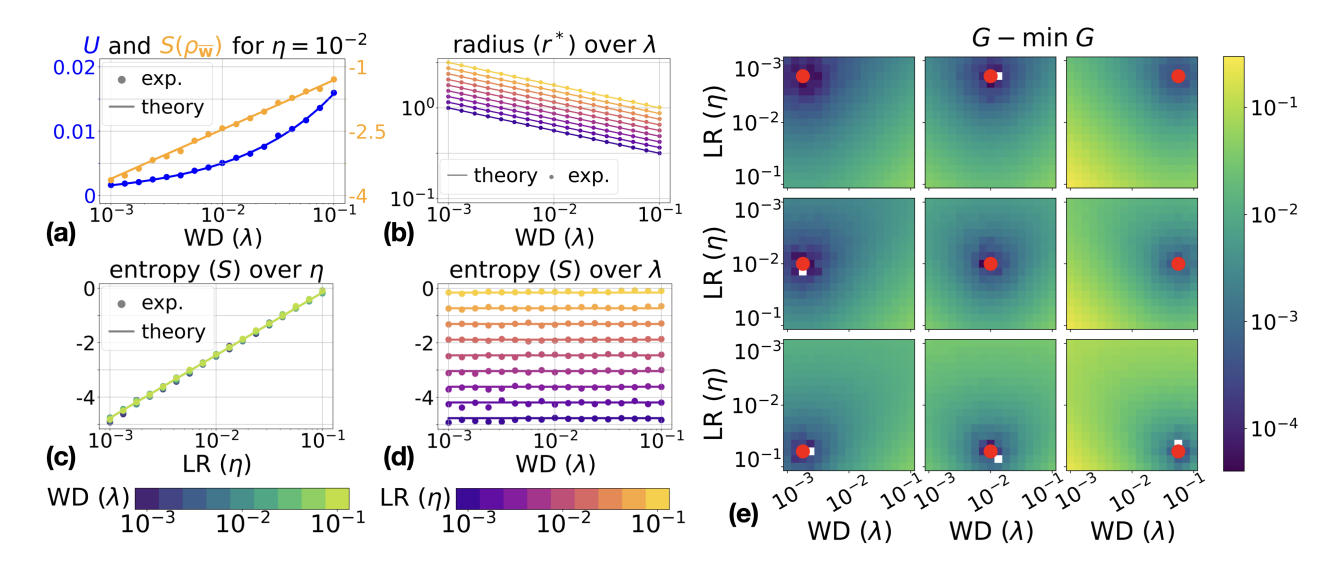


Figure 1: Results for the VMF isotropic noise model with fixed LR  $\eta$  and WD  $\lambda$ . Subfigures a-d: points are numerical measurements, solid lines are theoretical predictions:  $U = \frac{d-1}{2}T$ ,  $S(\rho_{\overline{w}}) = \frac{d-1}{2}\log(2\pi eT)$ ,  $S = S(\rho_{\overline{w}}) + (d-1)\log r^*$ , and  $r^* = \sqrt{\frac{T(d-1)}{p}}$ , with  $T = \sqrt{\frac{\eta\lambda\sigma^2}{2(d-1)}}$  and  $p = \lambda$ . Subfigure e: Gibbs energy minimization (V2). Each subplot corresponds to a fixed pair  $(\eta^*, \lambda^*)$ , denoted with red circle. The colormap shows the difference between G and its minimum across stationary distributions, with the minimizer marked by a white square. Ideally, red circles coincide with white squares; in practice, they either match or lie very close.

1987). Given a sample  $\{\boldsymbol{x}_1,\ldots,\boldsymbol{x}_N\}$  with  $\boldsymbol{x}_i \in \mathbb{R}^d$ , the estimator  $\hat{S}_{\mathbb{R}^d}$  is

$$\hat{S}_{\mathbb{R}^d}(\boldsymbol{x}) = \frac{d}{N} \sum_{i=1}^N \log \zeta_i + C(N, d), \tag{25}$$

where  $\zeta_i$  is the L2 distance from  $\boldsymbol{x}_i$  to its nearest neighbor and C(N,d) is the function of sample size and dimensionality. However, this estimator operates in the Euclidian space, while we are interested in the entropy  $S_{\mathbb{S}^{d-1}}(\overline{\boldsymbol{w}})$  on the unit sphere. To mitigate this mismatch, we convert  $\overline{\boldsymbol{w}}$  to spherical coordinates  $\boldsymbol{\theta} = \{\theta_1, \dots, \theta_{d-2}, \phi\}$ , estimate entropy of this angular vector with Eq. 25, and correct it by the expected Jacobian of the spherical coordinate transformation

$$\hat{S}_{\mathbb{S}^{d-1}}(\overline{\boldsymbol{w}}) = \hat{S}_{\mathbb{R}^{d-1}}(\boldsymbol{\theta}) + \mathbb{E}_{\rho_{\overline{\boldsymbol{w}}}} \Big[ \log J(\boldsymbol{\theta}) \Big], \qquad (26)$$

where 
$$\log J(\boldsymbol{\theta}) = \sum_{j=1}^{d-2} (d-1-j) \log \sin(\theta_j)$$
 (27)

The proof of this formula is provided in Appendix D.5. The total entropy is then

$$\hat{S}(\boldsymbol{w}) = \hat{S}_{\mathbb{S}^{d-1}}(\overline{\boldsymbol{w}}) + (d-1)\log \mathbb{E}\|\boldsymbol{w}\|$$
 (28)

In the experiments, we wait until the loss and radius stabilize during the training run. Then, we maintain a queue of 1000 weight vectors sampled every 50 iterations along the training trajectory to reduce correlation between consecutive samples.

**Results** In Figure 1, we present the results of numerical simulation. Subfigure 1a shows that both the average loss U and the entropy on the unit sphere  $S(\rho_{\overline{w}})$  match the analytical VMF predictions, providing a strong evidence, that this distribution is indeed stationary. Subfigures 1b and 1e validate **V1** and **V2**, respectively. To verify **V3**, we compute the partial derivatives of the total entropy S:

$$\left(\frac{\partial S}{\partial \log \eta}\right)_{\lambda} = \frac{d-1}{2}, \qquad \left(\frac{\partial S}{\partial \log \lambda}\right)_{\eta} = 0$$
 (29)

Subfigures 1c,d show that empirical measurements closely follow these theoretic predictions. For **V4**, we calculate the isochoric heat capacity

$$C_V = \left(\frac{\delta Q}{\mathrm{d}T}\right)_V = \left(\frac{\partial U}{\partial T}\right)_V = \frac{d-1}{2}$$
 (30)

Combining it with  $C_p - C_V = \frac{d-1}{2}$ , we get  $\gamma = \frac{C_p}{C_V} = 2$ . In the adiabatic process, we maintain  $pV^{\gamma} = \text{const}$ , which reduces to

$$pV^{\gamma} \propto p^{1-\gamma}T^{\gamma} \propto \eta^{\frac{\gamma}{2}} \lambda^{1-\frac{\gamma}{2}} \Big|_{\gamma=2} \propto \eta$$
 (31)

Therefore, keeping  $\eta$  fixed and varying  $\lambda$  yields an adiabatic process with  $\mathrm{d}S=0$ . This is indeed observed in the simulation (Subfigures 1c,d): the entropy depends only on  $\eta$  and remains constant as  $\lambda$  changes. Note that this property is specific to the VMF distribution. For other distributions  $\rho_{\overline{w}}$ , the values of  $C_V$ ,  $C_p$ , and  $\gamma$  may differ, requiring coordinated changes of  $\eta$  and  $\lambda$  to achieve an adiabatic process.

#### 6 Neural network experiments

#### 6.1 Generalizing isotropic noise model

The case of neural networks is complicated by the behavior of covariance matrix  $\Sigma_{\overline{w}}$ , which is both anisotropic and spatially dependent. Chaudhari and Soatto (2018) show that for general networks (i.e., not necessarily scale-invariant) trained with fixed LR  $\eta$ , the stationary distribution takes the form  $\rho_{w} \propto \exp(-\Phi(w)/T_{0})$  with  $T_{0} \propto \eta$ . Here  $\Phi(w)$  is no longer the training loss L(w), as in the isotropic noise model, but some implicit potential, determined by the training loss L(w) and the covariance matrix  $\Sigma_{w}$ , and independent of the LR  $\eta$ . Kunin et al. (2023) derive an explicit formula for this potential in linear regression. As the stationary distribution is of Gibbs form, the Helmholtz energy F is still minimized:

$$F = \mathbb{E}_{\rho_{\boldsymbol{w}}}[\Phi(\boldsymbol{w})] - T_0 S(\rho_{\boldsymbol{w}})$$
 (32)

We extend this logic to the unit sphere by defining  $\rho_{\overline{w}} \propto \exp(-\Phi(\overline{w})/T_0)$ , where  $T_0$  depends on training hyperparameters. This distribution arises in all three training protocols, considered in Section 3.2. Now, we assume that  $\operatorname{Tr} \Sigma_{\overline{w}} = \operatorname{const}$  for all  $\overline{w}$  (while the covariance matrix  $\Sigma_{\overline{w}}$  itself might be different). A similar assumption has been explored in Li et al. (2020) and Wan et al. (2021). Let  $\sigma^2 = \frac{1}{d-1} \operatorname{Tr} \Sigma_{\overline{w}}$ . Now, if we define  $T = \sigma^2 T_0$ , then the minimization of  $\mathbb{E}_{\rho_{\overline{w}}}[\Phi(\overline{w})] - T_0 S(\rho_{\overline{w}})$  is equivalent to minimizing

$$U(\rho_{\overline{w}}) - TS(\rho_{\overline{w}}), \text{ with } U = \mathbb{E}_{\rho_{\overline{w}}}[\sigma^2 \Phi(\overline{w})],$$
 (33)

which we consider as a new definition of the Helmholtz energy F. Note that, F is minimized on the unit sphere for all three cases, and minimization of Gibbs energy G arises if we consider both  $\rho_{\overline{w}}$  and  $r^*$ . Consequently, we define  $G = F + (d-1)\log r^* + \lambda \frac{(r^*)^2}{2}$ .

To summarize, these key differences in the thermodynamic analogy between neural networks and the isotropic noise model are:

- 1. The covariance matrix  $\Sigma_{\overline{w}}$  is anisotropic, so the energy function is not the training loss  $L(\overline{w})$ , but a potential  $\sigma^2\Phi(\overline{w})$  with no explicit form.
- 2. The formulae for temperature T and stationary radius  $r^*$  remain the same as in Section 3.2, but  $\sigma^2 = \frac{1}{d-1} \operatorname{Tr} \Sigma_{\overline{w}}$  replaces the isotropic variance.

Thus, the ideal gas laws still hold, and we expect the tests V1-V4 to hold. However, since  $\Phi$  is unknown, we can only directly verify V1 and V3.

#### 6.2 Experimental setup

We train ResNet-18 (He et al., 2016) on CIFAR-10 (Krizhevsky et al., 2009a) with varying LR  $\eta$  and WD  $\lambda$ , fixed batch size B = 128, for  $t = 10^6$  iterations. The entropy estimation queue stores 1000 vectors with new weights added every 25 iterations. All models are made fully scale-invariant following Li and Arora (2020). We also use a "thin" model with the width multiplier k = 4 (while the default value is k = 64), the resulting number of trainable parameters is d = 43692. This choice is motivated by (1) memory constraints for storing the weight queue for entropy estimation, and (2) larger number of trainable parameters leads to overparameterization, which imposes a specific behavior of stochastic gradients for small LRs in later stages of training (in fact, there is convergence to a minimum instead of stabilization at the stationary distribution). We discuss the results for overparameterized models in Appendix H. In the main text, we show the results only for the fixed LR case, two other training protocols are presented in the Appendix F. There we also provide results for the ConvNet architecture from Kodryan et al. (2022) and the CIFAR-100 dataset (Krizhevsky et al., 2009b).

Estimating entropy in high dimensions is challenging: the nearest-neighbor estimator is unbiased only asymptotically, with a bias of order  $\mathcal{O}(N^{-2/d})$  (Delattre and Fournier, 2017). We assume the bias is roughly constant across different stationary distributions, allowing accurate reconstruction of entropy derivatives for Maxwell relations. Empirically, **V3** holds with high precision, supporting this assumption.

#### 6.3 Results

We present the results in Figure 2. Subfigure 2a shows that  $\sigma^2$  varies across stationary distributions. While theory utilizes a fixed value for  $\sigma^2$ , in practice it depends on the hyperparameters and, notably, primarily on the product  $\eta\lambda$ . We therefore define temperature as  $T = \sqrt{\frac{\eta \lambda \sigma^2}{2(d-1)}}$  using the empirically measured  $\sigma^2$ . The resulting values of T are shown in Subfigure 2b. T generally increases with  $\eta$  and  $\lambda$ , but for large  $\lambda$  values it exhibits non-monotonic behavior. For example, when  $\lambda = 10^{-1}$ , T decreases for  $10^{-1} \le \eta \le 10^{0.5}$  and increases again for  $\eta \ge 10^{0.5}$ . This behavior arises from deviations in  $\sigma^2$  from the general trend observed for  $\eta \lambda < 10^{-2}$ . These results suggest that, for large  $\eta\lambda$ , stationary distributions explore regions of the weight space with different characteristics, consistent with prior observations by Sadrtdinov et al. (2024), who analyze the loss landscape under large LRs.

In Subfigure 2c, we show that the stationary radius

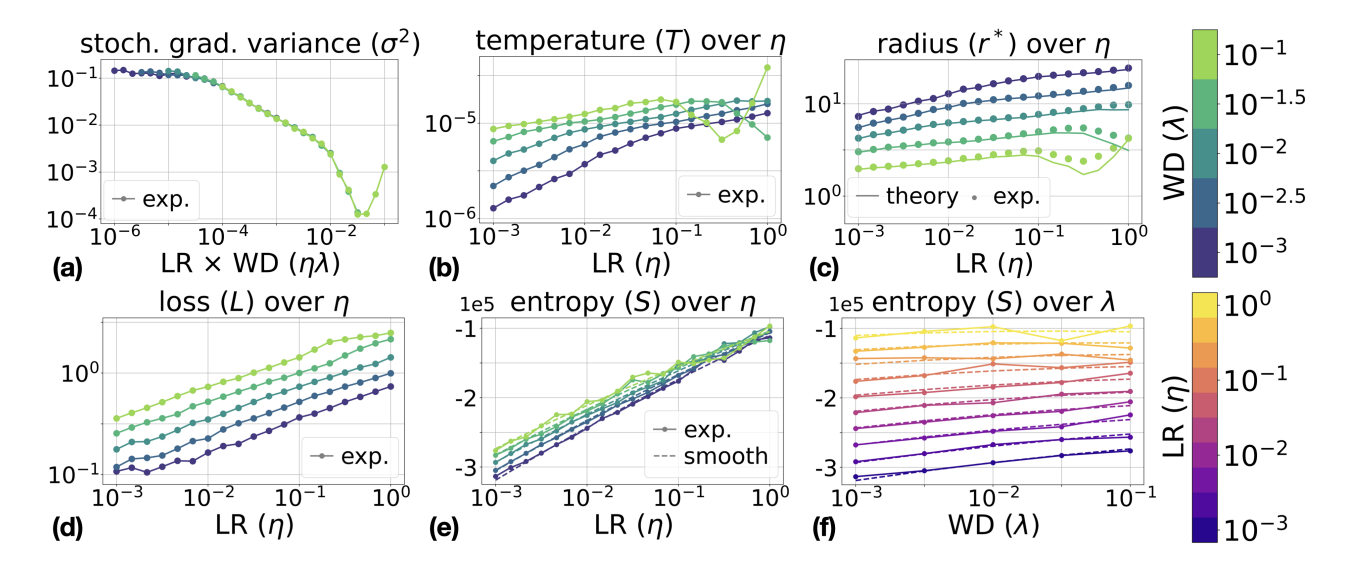


Figure 2: Results for ResNet-18 on CIFAR-10 with fixed LR  $\eta$  and WD  $\lambda$ . Subfigures a, b, d: empirically measured  $\sigma^2$ , mean loss L, and temperature T given by  $T = \sqrt{\frac{\eta \lambda \sigma^2}{2(d-1)}}$ , respectively. Subfigure c: stationary radius  $r^* = \sqrt{\frac{T(d-1)}{p}}$  (solid lines, theory) vs. experimental values (points). Subfigures e and f: entropy S as a function of  $\eta$  and  $\lambda$ ; solid lines with markers show experimental estimates, dashed lines their smoothed versions.

 $r^*$  closely follows its theoretic prediction, confirming V1. The mismatch becomes significant only for larger values of  $\eta$  and  $\lambda$ , which we refer to as the discretization error of SDE. This happens, because the continuous SDE model does not account for the norm of the mean (i.e., full-batch) gradient, which acts as centrifugal force, and thus leads to a larger stationary radius. In Appendix G, we derive a correction to the radius formula, which predicts the stationary  $r^*$  more accurately for larger values of  $\eta$  and  $\lambda$ .

Finally, to verify **V3**, we represent S as a function of  $\log \eta$  and  $\log \lambda$ , shown in Subfigures 2e and f. The empirical estimates are noisy, so we smooth them using the polynomial regression up to quadratic terms

$$S(\log \eta, \log \lambda) = a_0 + a_1 \log \eta + a_2 \log \lambda + a_3 \log^2 \eta + a_4 \log^2 \lambda + a_5 \log \eta \log \lambda$$
 (34)

We adopt a quadratic model since the lines of S vary in slope for different values of  $\lambda$  (Subfigure 2e), making a simpler linear regression insufficient, as it enforces identical slopes across  $\lambda$ . The quadratic approximation achieves the coefficient of determination  $R^2 \approx 0.9926$ . The resulting partial derivatives are

$$\left(\frac{\partial S}{\partial \log \eta}\right)_{\lambda} = a_1 + 2a_3 \log \eta + a_5 \log \lambda \qquad (35)$$

$$\left(\frac{\partial S}{\partial \log \lambda}\right)_{\eta} = a_2 + 2a_4 \log \lambda + a_5 \log \eta \qquad (36)$$

To satisfy Eq. 23, we need  $a_1-a_2=\frac{d-1}{2}$  and  $2a_3-a_5=2a_4-a_5=0$ . In the experiment, we get  $\frac{a_1-a_2}{(d-1)/2}\approx$ 

0.993 and  $\frac{2a_3-a_5}{(d-1)/2} \approx 0.005$ , and,  $\frac{2a_4-a_5}{(d-1)/2} \approx 0.005$  which leads to a maximal absolute error of < 2.5% between the left- and right-hand sides of Eq. 23 across  $\eta \in [10^{-3}, 10^0]$  and  $\lambda \in [10^{-3}, 10^{-1}]$ .

#### 7 Discussion

Extending ideal gas analogy Answering the question posed in the title of this paper, if the assumption  $\text{Tr}\,\Sigma_{\overline{w}}=\text{const}$  holds, the stationary behavior of SGD is fully consistent with the ideal gas, just like in the isotropic noise model. In practice, however, we observe that stationary values of  $\sigma^2$  vary with training hyperparameters. Despite this, our experiments demonstrate that V1 and V3 are still satisfied.

Developing a more general thermodynamic description that accounts for variable  $\operatorname{Tr} \Sigma_{\overline{w}}$  is an interesting direction for future work. One possible approach is to consider a real gas with the state equation  $V=Z(p,T)\frac{RT}{p}$ , where Z is the compressibility factor quantifying deviations from ideal gas behavior. This equation is analogous to  $\frac{(r^*)^2}{2}=\operatorname{Tr} \Sigma_{\overline{w}} \frac{\eta_{\rm eff}}{4\lambda}$  (which follows from Eq. 11), suggesting that an analogy between scale-invariant neural networks and a real gas could be as natural as the one established here between the isotropic noise model and the ideal gas.

Another promising direction is generalizing the analogy to non-scale-invariant networks. This requires reconsidering the definition of "volume", since our for-

mulation relies on the deterministic evolution of the parameter norm (Eq. 11, 18), which follows from scale invariance. Finally, extending the framework to more complex optimizers, such as SGD with momentum or Adam Kingma and Ba (2015), could provide insights directly applicable to common training practices.

**Practical implications** Our work adopts a thermodynamic perspective to better understand how training hyperparameters, specifically the learning rate and weight decay, influence the stationary distribution of SGD. In practice, neural networks are rarely trained with a fixed learning rate, and such thermodynamic insights may guide the development of more effective learning rate schedulers (Liu et al., 2025). One of the key outcomes of our framework is the emergence of Maxwell relations, which suggest a possible approach to designing schedulers that explicitly control the rate of entropy decay. Regulating entropy decay may ensure that the learning rate decreases at a pace that effectively decreases the training loss, while avoiding premature convergence to sharp minima often associated with poor generalization (Kodryan et al., 2022).

Furthermore, the training hyperparameters determine the temperature, which governs the trade-off between internal energy and entropy. This balance is crucial for weight averaging (Izmailov et al., 2018), a widely used technique to improve model performance, which averages the weights of several checkpoints along the training trajectory. While low training loss for each individual model is necessary for good accuracy, high entropy ensures diversity among models, which is essential for effective averaging. Selecting hyperparameters that optimize this balance is therefore non-trivial. Indeed, Sadrtdinov et al. (2024) show that the most effective learning rates for weight averaging often lie above the convergence threshold, where training loss and test accuracy are not optimal. Exploring how entropy dynamics influence the quality of weight averaging thus presents an intriguing direction for future research. The Maxwell relations quantify how entropy changes with hyperparameters, making them a useful tool for both theoretical and empirical studies of weight averaging.

#### 8 Conclusion

In this work, we introduced and empirically validated a thermodynamic framework for describing the stationary distributions of SGD in scale-invariant neural networks. We defined macroscopic thermodynamic variables and related them to learning rate, weight decay, and parameter norm. We rigorously showed that, under the simplified isotropic noise model, stationary distributions follow ideal gas laws. Importantly, the key predictions of this framework also hold in experiments with neural networks. Future work may extend this analogy to settings with variable noise, non-scale-invariant architectures, or more complex optimizers, and may further support principled approaches to hyperparameter tuning for learning rate scheduling and weight averaging.

#### Acknowledgments

We would like to thank Mikhail Burtsev for the valuable comments and discussions. We also thank Alexander Shabalin for insightful conversations and personal support. Ekaterina Lobacheva was supported by IVADO and the Canada First Research Excellence Fund. The authors gratefully acknowledge the computing time made available to them on the high-performance computer at the NHR Center of TU Dresden. This center is jointly supported by the Federal Ministry of Research, Technology and Space of Germany and the state governments participating in the NHR (www.nhr-verein.de/unsere-partner). The empirical results were enabled by compute resources and technical support provided by Mila - Quebec AI Institute (mila.quebec).

#### References

- Alemi, A. A. and Fischer, I. (2018). TherML: Thermodynamics of machine learning.
- Ali Mehmeti-Göpel, C. H. and Wand, M. (2024). On the weight dynamics of deep normalized networks. In *Proceedings of the 41st International Confer*ence on Machine Learning, volume 235 of *Proceed*ings of Machine Learning Research, pages 992–1007. PMLR.
- Arora, S., Li, Z., and Lyu, K. (2019). Theoretical analysis of auto rate-tuning by batch normalization. In *International Conference on Learning Represen*tations.
- Ba, J. L., Kiros, J. R., and Hinton, G. E. (2016). Layer normalization. arXiv preprint arXiv:1607.06450.
- Bjorck, N., Gomes, C. P., Selman, B., and Weinberger, K. Q. (2018). Understanding batch normalization. Advances in Neural Information Processing Systems, 31.
- Chaudhari, P., Choromanska, A., Soatto, S., LeCun, Y., Baldassi, C., Borgs, C., Chayes, J., Sagun, L., and Zecchina, R. (2017). Entropy-SGD: Biasing gradient descent into wide valleys. In *International Conference on Learning Representations*.
- Chaudhari, P. and Soatto, S. (2018). Stochastic gradient descent performs variational inference, converges

- to limit cycles for deep networks. In *International Conference on Learning Representations*.
- Chen, X., Liang, C., Huang, D., Real, E., Wang, K., Pham, H., Dong, X., Luong, T., Hsieh, C.-J., Lu, Y., and Le, Q. V. (2023). Symbolic discovery of optimization algorithms. In Advances in Neural Information Processing Systems.
- Chen, X., Soh, B. W., Ooi, Z.-E., Vissol-Gaudin, E., Yu, H., Novoselov, K. S., Hippalgaonkar, K., and Li, Q. (2024). Constructing custom thermodynamics using deep learning. *Nature Computational Science*, 4(1):66–85.
- Cho, M. and Lee, J. (2017). Riemannian approach to batch normalization. In *Proceedings of the 31st International Conference on Neural Information Processing Systems*, NIPS'17, page 5231–5241. Curran Associates Inc.
- Delattre, S. and Fournier, N. (2017). On the kozachenko-leonenko entropy estimator. *Journal of Statistical Planning and Inference*, 185:69–93.
- Du, S. S., Zhai, X., Poczos, B., and Singh, A. (2019). Gradient descent provably optimizes overparameterized neural networks. In *International Conference on Learning Representations*.
- Fioresi, R., Faglioni, F., Morri, F., and Squadrani, L. (2021). On the thermodynamic interpretation of deep learning systems. In Nielsen, F. and Barbaresco, F., editors, Geometric Science of Information, pages 909–917, Cham. Springer International Publishing.
- Gao, Y. and Chaudhari, P. (2020). A free-energy principle for representation learning. In *International Conference on Machine Learning*.
- He, K., Zhang, X., Ren, S., and Sun, J. (2016). Deep residual learning for image recognition. In Proceedings of the IEEE conference on computer vision and pattern recognition, pages 770–778.
- Hoffer, E., Banner, R., Golan, I., and Soudry, D. (2018). Norm matters: efficient and accurate normalization schemes in deep networks. Advances in Neural Information Processing Systems, 31.
- Ioffe, S. and Szegedy, C. (2015). Batch normalization: Accelerating deep network training by reducing internal covariate shift. In *International conference on machine learning*, pages 448–456. PMLR.
- Izmailov, P., Wilson, A., Podoprikhin, D., Vetrov, D., and Garipov, T. (2018). Averaging weights leads to wider optima and better generalization. In 34th Conference on Uncertainty in Artificial Intelligence 2018, UAI 2018, pages 876–885.
- Jastrzębski, S., Kenton, Z., Arpit, D., Ballas, N., Fischer, A., Bengio, Y., and Storkey, A. (2017). Three

- factors influencing minima in sgd. arXiv preprint arXiv:1711.04623.
- Kingma, D. P. and Ba, J. (2015). Adam: A method for stochastic optimization. In *International Conference* on Learning Representations.
- Kodryan, M., Lobacheva, E., Nakhodnov, M., and Vetrov, D. (2022). Training scale-invariant neural networks on the sphere can happen in three regimes. In Advances in Neural Information Processing Systems.
- Kohler, J., Daneshmand, H., Lucchi, A., Hofmann, T., Zhou, M., and Neymeyr, K. (2019). Exponential convergence rates for batch normalization: The power of length-direction decoupling in non-convex optimization. In Chaudhuri, K. and Sugiyama, M., editors, Proceedings of the Twenty-Second International Conference on Artificial Intelligence and Statistics, volume 89 of Proceedings of Machine Learning Research, pages 806–815. PMLR.
- Kosson, A., Messmer, B., and Jaggi, M. (2024). Rotational equilibrium: how weight decay balances learning across neural networks. In *Proceedings of the 41st International Conference on Machine Learning*, ICML'24. JMLR.org.
- Kozachenko, L. F. and Leonenko, N. N. (1987). Sample estimate of the entropy of a random vector. *Problems Inform. Transmission*, 23:95–101.
- Kozyrev, S. V. (2025). How to explain grokking.
- Krizhevsky, A., Nair, V., and Hinton, G. (2009a). CIFAR-10 (canadian institute for advanced research).
- Krizhevsky, A., Nair, V., and Hinton, G. (2009b). CIFAR-100 (canadian institute for advanced research).
- Kunin, D., Sagastuy-Brena, J., Gillespie, L., Margalit, E., Tanaka, H., Ganguli, S., and Yamins, D. L. K. (2023). The limiting dynamics of SGD: Modified loss, phase-space oscillations, and anomalous diffusion. *Neural Computation*, 36(1):151–174.
- Lapenna, M., Faglioni, F., and Fioresi, R. (2023). Thermodynamics modeling of deep learning systems for a temperature based filter pruning technique. *Frontiers in Physics*, Volume 11 2023.
- Le Ny, A. (2008). Introduction to (generalized) gibbs measures. *Ensaios Matemáticos*, 15(1-126).
- Li, Z. and Arora, S. (2020). An exponential learning rate schedule for deep learning. In *International Conference on Learning Representations*.
- Li, Z., Lyu, K., and Arora, S. (2020). Reconciling modern deep learning with traditional optimization analyses: The intrinsic learning rate. *Advances in Neural Information Processing Systems*, 33.

- Liu, Z., Liu, Y., Gore, J., and Tegmark, M. (2025). Neural thermodynamic laws for large language model training.
- Lobacheva, E., Kodryan, M., Chirkova, N., Malinin, A., and Vetrov, D. P. (2021). On the periodic behavior of neural network training with batch normalization and weight decay. In Advances in Neural Information Processing Systems.
- Loshchilov, I., Hsieh, C.-P., Sun, S., and Ginsburg, B. (2025). nGPT: Normalized transformer with representation learning on the hypersphere. In *The Thirteenth International Conference on Learning Representations*.
- Loshchilov, I. and Hutter, F. (2019). Decoupled weight decay regularization. In *International Conference on Learning Representations*.
- Lyle, C., Zheng, Z., Khetarpal, K., Martens, J., van Hasselt, H., Pascanu, R., and Dabney, W. (2024). Normalization and effective learning rates in reinforcement learning. In Advances in Neural Information Processing Systems, volume 37, pages 106440– 106473. Curran Associates, Inc.
- Ma, S., Bassily, R., and Belkin, M. (2018). The power of interpolation: Understanding the effectiveness of SGD in modern over-parametrized learning. In *International Conference on Machine Learning*.
- Mandt, S., Hoffman, M. D., and Blei, D. M. (2017). Stochastic gradient descent as approximate bayesian inference. J. Mach. Learn. Res., 18(1):4873–4907.
- Michela, L., Francesco, F., Rita, F., and Giovanni, B. (2025). Temperature-based pruning for input features in graph neural networks. *The European Physical Journal Plus*, 140(9):880.
- Nacson, M. S., Srebro, N., and Soudry, D. (2019). Stochastic gradient descent on separable data: Exact convergence with a fixed learning rate. In *International Conference on Artificial Intelligence and Statistics*.
- Olver, F. W. J., Olde Daalhuis, A. B., Lozier, D. W., Schneider, B. I., Boisvert, R. F., Clark, C. W., Miller, B. R., B. V. Saunders, H. S. C., and McClain, M. A. (2025). NIST Digital Library of Mathematical Functions. https://dlmf.nist.gov/, Release 1.2.4 of 2025-03-15.
- Sadrtdinov, I., Klimov, I., Lobacheva, E., and Vetrov, D. (2025). Sgd as free energy minimization: A thermodynamic view on neural network training.
- Sadrtdinov, I., Kodryan, M., Pokonechny, E., Lobacheva, E., and Vetrov, D. (2024). Where do large learning rates lead us? In *Advances in Neural Information Processing Systems*, volume 37, pages 58445–58479. Curran Associates, Inc.

- Santurkar, S., Tsipras, D., Ilyas, A., and Madry, A. (2018). How does batch normalization help optimization? Advances in Neural Information Processing Systems, 31.
- Sclocchi, A. and Wyart, M. (2024). On the different regimes of stochastic gradient descent. *Proceedings of the National Academy of Sciences*, 121(9):e2316301121.
- Smith, S. and Le, Q. V. (2018). A bayesian perspective on generalization and stochastic gradient descent. In *International Conference on Learning Represen*tations.
- Tishby, N. and Zaslavsky, N. (2015). Deep learning and the information bottleneck principle.
- Van Laarhoven, T. (2017). L2 regularization versus batch and weight normalization. arXiv preprint arXiv:1706.05350.
- Wan, R., Wang, Q., Zhang, X., Tai, Y.-W., Sun, J., and Tang, C.-K. (2023). How normalization and weight decay can affect SGD? insights from a simple normalized model.
- Wan, R., Zhu, Z., Zhang, X., and Sun, J. (2021). Spherical motion dynamics: Learning dynamics of normalized neural network using sgd and weight decay. In Ranzato, M., Beygelzimer, A., Dauphin, Y., Liang, P., and Vaughan, J. W., editors, Advances in Neural Information Processing Systems, volume 34, pages 6380–6391. Curran Associates, Inc.
- Wang, Y. and Wang, Z. (2022). Three-stage evolution and fast equilibrium for SGD with non-degerate critical points. In *Proceedings of the 39th International Conference on Machine Learning*, volume 162 of *Proceedings of Machine Learning Research*, pages 23092–23113. PMLR.
- Zhang, D. (2024). On the temperature of machine learning systems.
- Zhang, G., Wang, C., Xu, B., and Grosse, R. (2019).
  Three mechanisms of weight decay regularization.
  In International Conference on Learning Representations.
- Zhang, Y., Saxe, A. M., Advani, M. S., and Lee, A. A. (2018). Energy–entropy competition and the effectiveness of stochastic gradient descent in machine learning. *Molecular Physics*, 116(21-22):3214–3223.
- Ziyin, L., Xu, Y., and Chuang, I. (2025). Neural thermodynamics i: Entropic forces in deep and universal representation learning. arXiv preprint arXiv:2505.12387.
- Zou, D., Cao, Y., Zhou, D., and Gu, Q. (2018). Stochastic gradient descent optimizes overparameterized deep relu networks. arXiv preprint arXiv:1811.08888.

### Can Training Dynamics of Scale-Invariant Neural Networks Be Explained by the Thermodynamics of an Ideal Gas? Supplementary Materials

#### A TABLE OF NOTATIONS

In this section, we present Table 1 with general mathematical notations used in the paper and Table 2, which relates optimizational and thermodynamic quantities.

Object	Notation		
dimensionality (number of trainable parameters)	d		
identity matrix	$oldsymbol{I}_d$		
real Euclidian space	$\mathbb{R}^d$		
unit sphere embedded in $\mathbb{R}^d$	$\mathbb{S}^{d-1}$		
sphere of radius $r$ embedded in $\mathbb{R}^d$	$\mathbb{S}^{d-1}(r)$		
orthogonal projection matrix	$oldsymbol{P_x} = oldsymbol{I}_d - rac{oldsymbol{x} oldsymbol{x}^T}{\ oldsymbol{x}\ ^2}$		
standard Gaussian random vector	$oldsymbol{arepsilon} \sim \mathcal{N}(0,oldsymbol{I}_d)$		
standard Brownian motion in $\mathbb{R}^d$	$oldsymbol{B}_t$		
proportional to	$\propto$		
matrix trace	$\operatorname{Tr}$		
angular vector (spherical coordinates)	$\boldsymbol{\theta} = \{\theta_1, \dots, \theta_{d-2}, \phi\}$		
spherical coordinates transformation Jacobian	$J(\boldsymbol{\theta})$		

Table 1: General mathematical notations used throughout the paper.

#### B RELATED WORK

Thermodynamic perspective Several studies interpret the stochasticity of SGD through a thermodynamic lens by introducing a temperature parameter  $T \propto \eta/B$ , where  $\eta$  is the learning rate and B is the batch size. Grounded in SDE dynamics (Jastrzębski et al., 2017; Mandt et al., 2017), this temperature governs the noise magnitude in parameter updates, shaping different training regimes (Sclocchi and Wyart, 2024) (i.e., switching between stochastic and full-batch optimization) and convergence toward minima of varying sharpness (Smith and Le, 2018). Chaudhari and Soatto (2018) analyze the stationary Gibbs distribution  $\rho_{\boldsymbol{w}}(\boldsymbol{w}) \propto \exp(-\Phi(\boldsymbol{w})/T)$  and show that the potential  $\Phi(\boldsymbol{w})$  equals the training loss  $L(\boldsymbol{w})$  if and only if the stochastic gradient noise is isotropic. The stationary distribution  $\rho_{\boldsymbol{w}}$  also minimizes the (Helmholtz) free energy  $\mathbb{E}_{\rho_{\boldsymbol{w}}}[\Phi(\boldsymbol{w})] - TS(\rho_{\boldsymbol{w}})$ . Kunin et al. (2023) further derive the explicit form of  $\Phi(\boldsymbol{w})$  for linear regression trained using SGD with momentum and weight decay. We follow the same principle and treat temperature as a function of training hyperparameters, in our case, the learning rate  $\eta$  and weight decay  $\lambda$ . The thermodynamic interpretation of SGD offers valuable insights into practical training dynamics, including those observed in large language models (Liu et al., 2025), thereby helping to justify the use of specific learning rate schedulers.

An alternative approach estimates temperature empirically as the mean kinetic energy of individual parameters. (Fioresi et al., 2021) define a separate temperature for each network layer and show that its dependence on hyperparameters is more complex than the simple relation  $T \propto \eta/B$ . This idea supports pruning techniques that remove the "hottest" parameter groups: filters in convolutional networks (Lapenna et al., 2023) or input features in graph neural networks (Michela et al., 2025). Another approach is to derive temperature directly

Table 2: Notations used throughout the paper. Left column shows quantities from optimization, right column presents analogous variables from thermodynamics (if applicable).

OPTIMIZATION	THERMODYNAMICS					
Weight vector and microstates						
weight vector $\boldsymbol{w}$	microstate $i$					
unit direction vector $\overline{m{w}} = m{w}/\ m{w}\ $	<del>_</del>					
isotropic noise model: scale-invariant loss function $L(w) = L(\overline{w})$ anisotropic noise model: potential $\Phi(\overline{w})$	microstate energy $E_i$					
$\text{radius } r = \  \boldsymbol{w} \ $	<del></del>					
stationary radius $r^*$	<u> </u>					
Stationary distribution, internal energ	y and entropy					
stationary distribution (on $\mathbb{S}^{d-1}$ ) $\rho_{\overline{w}}(\overline{w}) \propto \exp\left(-\frac{L(\overline{w})}{T}\right)$ stationary distribution (on $\mathbb{S}^{d-1}(r^*)$ ) $\rho_{\boldsymbol{w}}(\boldsymbol{w}) = \rho_{\overline{\boldsymbol{w}}}(\overline{\boldsymbol{w}})\delta(r-r^*)$ internal energy $U = \mathbb{E}_{\rho_{\overline{\boldsymbol{w}}}}[L(\overline{\boldsymbol{w}})]$ entropy (on $\mathbb{S}^{d-1}$ ) $S(\rho_{\overline{\boldsymbol{w}}}) = \mathbb{E}_{\rho_{\overline{\boldsymbol{w}}}}[-\log \rho_{\overline{\boldsymbol{w}}}]$ entropy (on $\mathbb{S}^{d-1}(r^*)$ ) $S(\rho_{\boldsymbol{w}}) = S(\rho_{\overline{\boldsymbol{w}}}) + (d-1)\log r^*$	Gibbs distribution $p_i \propto \exp\left(-\frac{E_i}{T}\right)$ internal energy $U = \mathbb{E}_{p_i}[E_i]$ — entropy $S = \mathbb{E}_{p_i}[-\log p_i]$					
Variance of stochastic gradients						
covariance matrix of stochastic gradients $\Sigma_w, \Sigma_{\overline{w}}$ scalar variance of stochastic gradients $\sigma^2$ minibatch of data $\mathcal{B}$	_ _ _					
Training hyperparameters and macroscop	oic state variables					
weight decay coefficient (WD) $\lambda$	pressure $p$					
squared radius $\frac{r^2}{2}$	$ volume \ V $					
learning rate (LR) $\eta$	_					
effective learning rate (ELR) $\eta_{\text{eff}} = \eta/r^2$						
fixed sphere/fixed ELR: $T = \frac{\eta_{\rm eff}\sigma^2}{2}$ fixed LR: $T = \sqrt{\frac{\eta\lambda\sigma^2}{2(d-1)}}$	temperature $T$					
Thermodynamic potentials						
fixed $T, V$ : Helmholtz (free) energy $F$ fixed $T, V$ : Maxwell relation $\left(\frac{\partial S}{\partial V}\right)_T$						
fixed $T$ , $p$ : Gibbs (free) energy $G = U$ fixed $T$ , $p$ : Maxwell relation $\left(\frac{\partial S}{\partial p}\right)_T$	$ -TS + pV  = \left(\frac{\partial V}{\partial T}\right)_p $					
Ideal gas law						
dimensionality constant $\frac{d-1}{2}$	gas constant $R$					
fixed ELR $r^* = \sqrt{\frac{\eta_{\text{eff}}\sigma^2(d-1)}{2\lambda}}$ fixed LR $r^* = \sqrt[4]{\frac{\eta\sigma^2(d-1)}{2\lambda}}$	ideal gas law $V = \frac{RT}{p}$					
Adiabatic process						

heat Q

First Law of Thermodynamics  $\mathrm{d}U = \delta Q - p \mathrm{d}V$  isochoric heap capacity  $C_V = \left(\frac{\delta Q}{\mathrm{d}T}\right)_V = \left(\frac{\partial U}{\partial T}\right)_V$  isobaric heap capacity  $C_p = \left(\frac{\delta Q}{\mathrm{d}T}\right)_p$  adiabatic constant  $\gamma = C_p/C_V$ 

from free energy minimization. Sadrtdinov et al. (2025) treat the training loss as the internal energy and define temperature as a non-linear, monotonically increasing function of the learning rate, which empirically minimizes the free energy functional.

Beyond SGD dynamics, thermodynamic perspectives have also been applied to generalization. Some works define temperature via the parameter-to-data ratio (Zhang et al., 2018), while others treat it as an explicit hyperparameter encouraging convergence to flatter, more generalizable minima (Chaudhari et al., 2017). Similar analogies appear in representation learning (Alemi and Fischer, 2018; Gao and Chaudhari, 2020; Ziyin et al., 2025), particularly through the Information Bottleneck principle (Tishby and Zaslavsky, 2015), which formalizes the trade-off between compression and predictive power of learned features.

Scale-invariant neural networks Normalization layers, such as BatchNorm (Ioffe and Szegedy, 2015) and LayerNorm (Ba et al., 2016), are indispensable in modern neural architectures. They smooth the loss land-scape (Santurkar et al., 2018) and make training faster (Kohler et al., 2019) and more stable (Bjorck et al., 2018). Beyond these benefits, normalization layers induce scale invariance in network parameters, fundamentally altering their optimization dynamics. Arora et al. (2019) show that BatchNorm implicitly tunes the learning rate, while Hoffer et al. (2018) demonstrate that the weight direction evolves according to an effective learning rate  $\eta/\|\boldsymbol{w}\|^2$ . Van Laarhoven (2017) argue that, in scale-invariant networks, weight decay does not serve as a regularizer but instead controls the learning rate through the parameter norm, a phenomenon also confirmed by Zhang et al. (2019) and Li and Arora (2020).

Another line of research examines the equilibrium behavior of scale-invariant networks. Wan et al. (2021) establish conditions under which the weight norm converges. Using the SDE framework, Li et al. (2020); Wang and Wang (2022); Wan et al. (2023) describe the dynamics of such networks and show that the stationary distribution depends on the intrinsic learning rate  $\eta\lambda$ . Lobacheva et al. (2021) reveal that scale-invariant networks can exhibit periodic instabilities, while Kodryan et al. (2022) study the networks constrained to a fixed sphere and report different regimes: convergence, chaotic equilibrium, or divergence, which depend on the effective learning rate. Finally, Kosson et al. (2024) extend these findings to modern optimizers such as AdamW (Loshchilov and Hutter, 2019) and Lion (Chen et al., 2023).

Our framework In this work, we extend the previously established analogies between SGD dynamics and thermodynamics. Whereas prior studies primarily focused on quantities such as energy, entropy, and temperature, we demonstrate that the optimization of scale-invariant networks naturally gives rise to a richer thermodynamic framework, one that also admits well-defined notions of pressure and volume, and consequently, a direct analogy to the ideal gas law.

#### C INTRODUCTION TO THERMODYNAMICS

Thermodynamic state variables Thermodynamics focuses on systems made up of vast numbers of microscopic particles that move and interact with one another. Although the motion of individual particles is highly chaotic, their collective behavior exhibits statistical regularities, which permit a description in terms of macroscopic state variables. One key quantity is the internal energy U, the total kinetic and potential energy of all the particles in the system. Other fundamental variables include the entropy S, which measures the system's disorder, as well as temperature T, pressure p, and volume V. These variables naturally form two pairs of conjugates: (S,T) and (p,V). To fully specify the state of a thermodynamic system, one typically fixes one variable from each pair; these are referred to as the system's natural variables.

First and Second Law of Thermodynamics The First Law of Thermodynamics establishes the principle of energy conservation in thermodynamic processes. Its differential form is  $\mathrm{d}U = \delta Q - p \mathrm{d}V$ , where  $\delta Q^3$  denotes the infinitesimal heat supplied to the system. The Second Law of Thermodynamics introduces the concept of irreversibility and establishes the direction of spontaneous processes. For any isolated system (i.e.,  $\delta Q = 0$ ), the entropy satisfies  $\mathrm{d}S \geq 0$ , with equality holding only at equilibrium. This expresses the fact that thermodynamic systems spontaneously evolve toward equilibrium states, where entropy reaches a maximum under the given constraints. For non-isolated systems exchanging heat  $\delta Q$  with the environment, the second law generalizes to  $\mathrm{d}S \geq \delta Q/T$ , which accounts for entropy changes due to heat transfer and ensures that the total entropy, including

 $<sup>^{3}</sup>Q$  is not a state variable, like U or S, thus we write  $\delta Q$  instead of dQ.

that of the environment, does not decrease. Here, equality  $dS = \delta Q/T$  holds only for reversible processes, while for irreversible processes the inequality is strict. For a reversible process, the First Law can also be written as dU = TdS - pdV.

Thermodynamic potentials The equation dU = TdS - pdV enables the definition of thermodynamic potentials, which describe equilibrium under different sets of natural variables. At constant temperature T and volume V, the Helmholtz (free) energy F = U - TS is minimized at equilibrium. At constant temperature T and pressure p, the Gibbs (free) energy G = U - TS + pV reaches its minimum. This minimization principle directly follows from the Second Law, as  $dS \geq 0$  implies that free energies decrease in spontaneous processes until equilibrium is attained.

The differential forms of thermodynamic potentials yield the  $Maxwell\ relations$ , which link different thermodynamic derivatives. The differentials dF and dG can be expressed as (see Appendix D.2 for proofs)

$$dF = -SdT - pdV dG = -SdT + Vdp (37)$$

From dF = -SdT - pdV, it follows that  $\frac{\partial F}{\partial T} = -S$ ,  $\frac{\partial F}{\partial V} = -p$ , and one obtains

$$\left(\frac{\partial S}{\partial V}\right)_T = -\frac{\partial}{\partial V}\left(\frac{\partial F}{\partial T}\right) = -\frac{\partial}{\partial T}\left(\frac{\partial F}{\partial V}\right) = \left(\frac{\partial p}{\partial T}\right)_V,\tag{38}$$

while from dG = -SdT + Vdp, we have  $\frac{\partial G}{\partial T} = -S, \frac{\partial G}{\partial p} = V$ , and thus

$$-\left(\frac{\partial S}{\partial p}\right)_{T} = \frac{\partial}{\partial p}\left(\frac{\partial G}{\partial T}\right) = \frac{\partial}{\partial T}\left(\frac{\partial G}{\partial p}\right) = \left(\frac{\partial V}{\partial T}\right)_{p} \tag{39}$$

Maxwell relations allow experimental determination of entropy changes, which are otherwise difficult to measure directly.

**Gibbs distribution** On the microscopic scale, the *Gibbs distribution* connects thermodynamics with statistical mechanics. It assigns the probability  $p_i$  for the system to occupy a microstate i with energy  $E_i$ :

$$p_i = \frac{e^{-E_i/T}}{Z}, \qquad Z = \sum_i e^{-E_i/T}$$
 (40)

Temperature appears in the denominator of the exponential, controlling how energy is distributed among accessible states: lower temperatures concentrate probability on low-energy states, while higher temperatures produce a more uniform distribution.

Ideal gas and adiabatic process An ideal gas is a theoretical model of a gas in which intermolecular interactions are neglected and the internal energy depends only on temperature, with the dependence being linear,  $U \propto T$ . Its macroscopic behavior is described by the ideal gas law: pV = RT, where R is the gas constant. The heat capacity quantifies the amount of heat required to change the system's temperature. Commonly used are the isochoric heat capacity  $C_V = \begin{pmatrix} \frac{\delta Q}{dT} \end{pmatrix}_V = \begin{pmatrix} \frac{\partial U}{\partial T} \end{pmatrix}_V$  and the isobaric heat capacity  $C_p = \begin{pmatrix} \frac{\delta Q}{dT} \end{pmatrix}_p = \begin{pmatrix} \frac{\partial U}{\partial T} \end{pmatrix}_p + p \begin{pmatrix} \frac{\partial V}{\partial T} \end{pmatrix}_p$ , which for an ideal gas are constants and satisfy  $C_p - C_V = R$ . An important class of transformations is the adiabatic process, in which no heat is exchanged with the surroundings  $(\delta Q = 0)$ . For an adiabatic process, the First Law reduces to dU = -pdV, and the pressure and volume are related by  $pV^{\gamma} = \text{const}$  with  $\gamma = \frac{C_p}{C_V}$ . Moreover, if the process is reversible, we have  $dS = \delta Q/T = 0$ , meaning that we have the same entropy for different configurations of p and V.

#### D MISSING PROOFS

#### D.1 Derivation of SDE

SGD on a fixed sphere / with fixed ELR We begin by considering two training protocols that both employ a fixed ELR. First, we derive the SDE corresponding to the fixed ELR setting. Then, we reuse the resulting

equation for  $\overline{W}_t$  to describe training constrained to a fixed sphere, since the dynamics of the direction vector are independent of the projection onto the sphere. The SGD updates in the fixed ELR case are given by

$$\boldsymbol{w}_{k+1} = \boldsymbol{w}_k - \eta_{\text{eff}} \|\boldsymbol{w}_k\|^2 \left( \nabla L_{\mathcal{B}_k}(\boldsymbol{w}_k) + \lambda \boldsymbol{w}_k \right) = \boldsymbol{w}_k - \eta_{\text{eff}} \|\boldsymbol{w}_k\|^2 \left( \nabla L(\boldsymbol{w}_k) + \lambda \boldsymbol{w}_k \right) - \eta_{\text{eff}} \|\boldsymbol{w}_k\|^2 \left( \boldsymbol{\Sigma}_{\boldsymbol{w}} \right)^{1/2} \boldsymbol{\varepsilon}, \quad (41)$$

where  $\varepsilon \sim \mathcal{N}(0, I_d)$ . Similarly to Li et al. (2020), this discrete dynamics leads to the following SDE:

$$d\mathbf{W}_{t} = -\eta_{\text{eff}} \|\mathbf{W}_{t}\|^{2} \left(\nabla L(\mathbf{W}_{t}) + \lambda \mathbf{W}_{t}\right) dt + \eta_{\text{eff}} \|\mathbf{W}_{t}\|^{2} \left(\mathbf{\Sigma}_{\mathbf{W}_{t}}\right)^{\frac{1}{2}} d\mathbf{B}_{t}$$
(42)

To analyze the dynamics of the radius and the direction vector, we utilize the Ito's formula, which produces a new SDE describing the evolution of a twice-differentiable function  $f(t, \mathbf{x})$  when substituting  $\mathbf{x} = \mathbf{W}_t$ . Given an original SDE

$$dW_t = \mu(t, W_t)dt + G(t, W_t)dB_t$$
(43)

with  $\boldsymbol{\mu}: \mathbb{R} \times \mathbb{R}^d \to \mathbb{R}^d$  and  $\boldsymbol{G}: \mathbb{R} \times \mathbb{R}^d \to \mathbb{R}^{d \times d}$ , we can write a new SDE for  $f(t, \boldsymbol{W}_t)$  (we omit the dependence on t and  $\boldsymbol{W}_t$  for clarity)

$$df_t = \frac{\partial f}{\partial t} dt + \sum_{i=1}^d \frac{\partial f}{\partial x_i} \mu_i dt + \sum_{i,j=1}^d \frac{\partial f}{\partial x_i} G_{ij} d(\boldsymbol{B}_t)_j + \frac{1}{2} \sum_{i,j=1}^d \frac{\partial^2 f}{\partial x_i \partial x_j} (\boldsymbol{G} \boldsymbol{G}^T)_{ij} dt,$$
(44)

The last term is called the *Ito's correction term* and expresses extra drift from the function's curvature interacting with stochastic noise. An equivalent of Eq. 44 in the matrix notation is

$$df_t = \left(\frac{\partial f}{\partial t} + (\nabla_{\boldsymbol{x}} f)^T \boldsymbol{\mu} + \frac{1}{2} \operatorname{Tr} \left[ \boldsymbol{G} \boldsymbol{G}^T \nabla_{\boldsymbol{x}}^2 f \right] \right) dt + (\nabla_{\boldsymbol{x}} f)^T \boldsymbol{G} d\boldsymbol{B}_t$$
 (45)

We apply the Ito's formula for  $r(t, \boldsymbol{x}) = \|\boldsymbol{x}\|$  and  $\overline{\boldsymbol{x}}(t, \boldsymbol{x}) = \boldsymbol{x}/\|\boldsymbol{x}\|$ . Strictly speaking, these functions are not smooth at the origin; therefore, the origin must be excluded from consideration. In other words, the resulting SDEs are valid only when  $\|\boldsymbol{W}_t\| \ge \epsilon$  for some small  $\epsilon > 0$ . The derivatives of r are

$$\frac{\partial r}{\partial t} = 0, \quad \nabla_{\boldsymbol{x}} r = \frac{\boldsymbol{x}}{\|\boldsymbol{x}\|}, \quad \nabla_{\boldsymbol{x}}^2 r = \frac{\mathrm{d}}{\mathrm{d}\boldsymbol{x}} \left( \frac{\boldsymbol{x}}{\|\boldsymbol{x}\|} \right) = \frac{1}{\|\boldsymbol{x}\|} \boldsymbol{I}_d - \frac{\boldsymbol{x} \boldsymbol{x}^T}{\|\boldsymbol{x}\|^3} = \frac{1}{\|\boldsymbol{x}\|} \left( \boldsymbol{I}_d - \frac{\boldsymbol{x} \boldsymbol{x}^T}{\|\boldsymbol{x}\|^2} \right) = \frac{1}{\|\boldsymbol{x}\|} \boldsymbol{P}_{\boldsymbol{x}}$$
(46)

The Ito's correction term is

$$\frac{1}{2} \sum_{ij} \frac{\partial^{2} r}{\partial x_{i} \partial x_{j}} (\eta_{\text{eff}}^{2} \| \boldsymbol{x} \|^{4} \boldsymbol{\Sigma}_{\boldsymbol{x}})_{ij} = \frac{\eta_{\text{eff}}^{2} \| \boldsymbol{x} \|^{3}}{2} \sum_{ij} (\boldsymbol{P}_{\boldsymbol{x}})_{ij} (\boldsymbol{\Sigma}_{\boldsymbol{x}})_{ij} = \frac{\eta_{\text{eff}}^{2} \| \boldsymbol{x} \|^{3}}{2} \operatorname{Tr} \left( \boldsymbol{P}_{\boldsymbol{x}}^{T} \boldsymbol{\Sigma}_{\boldsymbol{x}} \right) = \frac{\eta_{\text{eff}}^{2} \| \boldsymbol{x} \|}{2} \operatorname{Tr} \left( \boldsymbol{P}_{\boldsymbol{x}}^{T} \boldsymbol{\Sigma}_{\overline{\boldsymbol{x}}} \right) = \frac{\eta_{\text{eff}}^{2} \| \boldsymbol{x} \|}{2} \operatorname{Tr} \left( \boldsymbol{I}_{d} - \overline{\boldsymbol{x}} \, \overline{\boldsymbol{x}}^{T} \right) \boldsymbol{\Sigma}_{\overline{\boldsymbol{x}}} \right) = \frac{\eta_{\text{eff}}^{2} \| \boldsymbol{x} \|}{2} \operatorname{Tr} \boldsymbol{\Sigma}_{\overline{\boldsymbol{x}}} - \frac{\eta_{\text{eff}}^{2} \| \boldsymbol{x} \|}{2} \operatorname{Tr} \left( \overline{\boldsymbol{x}}^{T} \boldsymbol{\Sigma}_{\overline{\boldsymbol{x}}} \overline{\boldsymbol{x}} \right) = \frac{\eta_{\text{eff}}^{2} \| \boldsymbol{x} \|}{2} \operatorname{Tr} \boldsymbol{\Sigma}_{\overline{\boldsymbol{x}}}$$

$$(47)$$

The second trace is nullified due to Eq. 5. Therefore, the SDE for radius is

$$dr_{t} = \left(\frac{\partial r_{t}^{t}}{\partial t} - \frac{\eta_{\text{eff}} \|\mathbf{W}_{t}\|^{2}}{\|\mathbf{W}_{t}\|^{2}} \mathbf{\underline{W}}_{t}^{T} \nabla L(\mathbf{W}_{t}) - \frac{\eta_{\text{eff}} \|\mathbf{W}_{t}\|^{2}}{\|\mathbf{W}_{t}\|} \lambda \mathbf{W}_{t}^{T} \mathbf{W}_{t} + \frac{\eta_{\text{eff}}^{2} \|\mathbf{W}_{t}\|}{2} \operatorname{Tr} \mathbf{\Sigma}_{\overline{\mathbf{W}}_{t}}\right) dt +$$

$$+ \frac{\eta_{\text{eff}} \|\mathbf{W}_{t}\|^{2}}{\|\mathbf{W}_{t}\|} \left( (\mathbf{\Sigma}_{\mathbf{W}_{t}})^{\frac{1}{2}} \mathbf{W}_{t}^{T} \right)^{T} d\mathbf{B}_{t} = \left( -\eta_{\text{eff}} \lambda r_{t}^{3} + \frac{\eta_{\text{eff}}^{2} r_{t}}{2} \operatorname{Tr} \mathbf{\Sigma}_{\overline{\mathbf{W}}_{t}} \right) dt$$

$$(48)$$

Now, the derivatives of  $\overline{x}$  (here  $\delta$  denotes the Kronecker delta)

$$\frac{\partial \overline{\boldsymbol{x}}}{\partial t} = 0, \qquad \frac{\partial \overline{\boldsymbol{x}}_k}{\partial x_i} = \frac{1}{\|\boldsymbol{x}\|} (\boldsymbol{P_x})_{ik} = \frac{\delta_{ik}}{\|\boldsymbol{x}\|} - \frac{x_i x_k}{\|\boldsymbol{x}\|^3}, \qquad \frac{\partial}{\partial x_j} \left(\frac{\delta_{ik}}{\|\boldsymbol{x}\|}\right) = -\frac{\delta_{ik} x_j}{\|\boldsymbol{x}\|^3}$$
(49)

$$\frac{\partial}{\partial x_{j}} \left( \frac{x_{i} x_{k}}{\|\boldsymbol{x}\|^{3}} \right) = \frac{\|\boldsymbol{x}\|^{3}}{\|\boldsymbol{x}\|^{6}} \left( \frac{\partial x_{i}}{\partial x_{j}} x_{k} + \frac{\partial x_{k}}{\partial x_{j}} x_{i} \right) - \frac{x_{i} x_{k} \cdot \frac{3}{2} \|\boldsymbol{x}\| \cdot 2x_{j}}{\|\boldsymbol{x}\|^{6}} = \frac{\delta_{ij} x_{k} + \delta_{kj} x_{i}}{\|\boldsymbol{x}\|^{3}} - \frac{3x_{i} x_{j} x_{k}}{\|\boldsymbol{x}\|^{5}}$$
(50)

$$\frac{\partial^2 \overline{x}_k}{\partial x_i \partial x_j} = \frac{3x_i x_j x_k}{\|\boldsymbol{x}\|^5} - \frac{\delta_{ij} x_k + \delta_{ki} x_j \delta_{kj} x_i}{\|\boldsymbol{x}\|^3}$$

$$(51)$$

The Ito's correction term for  $\overline{x}_k$  is

$$\frac{1}{2} \sum_{ij} \frac{\partial^2 \overline{x}_k}{\partial x_i \partial x_j} (\eta_{\text{eff}}^2 || \boldsymbol{x} ||^4 \boldsymbol{\Sigma}_{\boldsymbol{x}})_{ij}$$
(52)

Expanding each part separately

$$\sum_{ij} \delta_{ij} x_k(\mathbf{\Sigma}_{\mathbf{x}})_{ij} = x_k \sum_{ij} \delta_{ij}(\mathbf{\Sigma}_{\mathbf{x}})_{ij} = x_k \operatorname{Tr} \mathbf{\Sigma}_{\mathbf{x}}$$
(53)

$$\sum_{ij} \delta_{ik} x_j (\mathbf{\Sigma}_{\mathbf{x}})_{ij} = \sum_{j} x_j (\mathbf{\Sigma}_{\mathbf{x}})_{kj} = (\Sigma_{\mathbf{x}} \mathbf{x})_k = 0$$
(54)

$$\sum_{ij} \delta_{kj} x_i(\mathbf{\Sigma}_{\mathbf{x}})_{ij} = \sum_{i} x_i(\mathbf{\Sigma}_{\mathbf{x}})_{ik} = (\Sigma_{\mathbf{x}} \mathbf{x})_k = 0$$
(55)

$$3\sum_{ij} x_i x_j x_k(\mathbf{\Sigma}_{\boldsymbol{x}})_{ij} = 3x_k \sum_{ij} x_i x_j(\mathbf{\Sigma}_{\boldsymbol{x}})_{ij} = 3x_k(\boldsymbol{x}^T \mathbf{\Sigma}_{\boldsymbol{x}} \boldsymbol{x}) = 0$$
(56)

For the overall direction vector  $\overline{x}$ , the Ito's correction is

$$-\frac{\eta_{\text{eff}}^2 \|\boldsymbol{x}\|}{2} \boldsymbol{x} \operatorname{Tr} \boldsymbol{\Sigma}_{\boldsymbol{x}} = -\frac{\eta_{\text{eff}}^2 \|\boldsymbol{x}\|^2}{2} \overline{\boldsymbol{x}} \operatorname{Tr} \boldsymbol{\Sigma}_{\boldsymbol{x}} = -\frac{\eta_{\text{eff}}^2}{2} \overline{\boldsymbol{x}} \operatorname{Tr} \boldsymbol{\Sigma}_{\overline{\boldsymbol{x}}}$$
(57)

The resulting SDE for the direction vector is

$$d\overline{\boldsymbol{W}}_{t} = \left(\frac{\partial \overline{\boldsymbol{x}}}{\partial t} - \frac{\eta_{\text{eff}} \|\boldsymbol{W}_{t}\|^{2}}{\|\boldsymbol{W}_{t}\|} \boldsymbol{P}_{\boldsymbol{W}_{t}} \nabla L(\boldsymbol{W}_{t}) - \frac{\eta_{\text{eff}} \|\boldsymbol{W}_{t}\|^{2}}{\|\boldsymbol{W}_{t}\|} \boldsymbol{\lambda} \boldsymbol{P}_{\boldsymbol{W}_{t}} \boldsymbol{W}_{t}^{-0} - \frac{\eta_{\text{eff}}^{2}}{2} \operatorname{Tr} \left(\boldsymbol{\Sigma}_{\overline{\boldsymbol{W}}_{t}}\right) \overline{\boldsymbol{W}}_{t}\right) dt + \frac{\eta_{\text{eff}} \|\boldsymbol{W}_{t}\|^{2}}{\|\boldsymbol{W}_{t}\|} \boldsymbol{P}_{\boldsymbol{W}_{t}} \left(\boldsymbol{\Sigma}_{\boldsymbol{W}_{t}}\right)^{\frac{1}{2}} d\boldsymbol{B}_{t} = -\left(\eta_{\text{eff}} \nabla L(\overline{\boldsymbol{W}_{t}}) + \frac{\eta_{\text{eff}}^{2}}{2} \operatorname{Tr} \left(\boldsymbol{\Sigma}_{\overline{\boldsymbol{W}}_{t}}\right) \overline{\boldsymbol{W}}_{t}\right) dt + \eta_{\text{eff}} \left(\boldsymbol{\Sigma}_{\overline{\boldsymbol{W}}_{t}}\right)^{\frac{1}{2}} d\boldsymbol{B}_{t}$$

$$(58)$$

One may notice that the Ito's correction term gives a component, which is counter to the direction vector (i.e., it is of the form  $-\alpha \overline{W}_t$ , where  $\alpha$  is a positive scalar). This component is required to preserve the norm  $\|\overline{W}_t\|^2 = 1$  in the Ito formulation. Indeed, if we write down the squared norm after the update:

$$\|\overline{\boldsymbol{W}}_t + d\overline{\boldsymbol{W}}_t\|^2 = \|\overline{\boldsymbol{W}}_t\|^2 + 2\langle \overline{\boldsymbol{W}}_t, d\overline{\boldsymbol{W}}_t \rangle + \|d\overline{\boldsymbol{W}}_t\|^2 =$$
(59)

$$= \|\overline{\boldsymbol{W}}_{t}\|^{2} \underbrace{-2\eta_{\text{eff}}\overline{\boldsymbol{W}}_{t}^{T}\nabla L(\overline{\boldsymbol{W}}_{t})dt - \eta_{\text{eff}}^{2}\operatorname{Tr}\left(\boldsymbol{\Sigma}_{\overline{\boldsymbol{W}}_{t}}\right)\|\overline{\boldsymbol{W}}_{t}\|^{2}dt + 2\eta_{\text{eff}}\overline{\boldsymbol{W}}_{t}^{T}\left(\boldsymbol{\Sigma}_{\overline{\boldsymbol{W}}_{t}}\right)^{\frac{1}{2}}d\boldsymbol{B}_{t} + \underbrace{\eta_{\text{eff}}^{2}\|(\boldsymbol{\Sigma}_{\overline{\boldsymbol{W}}_{t}})^{\frac{1}{2}}d\boldsymbol{B}_{t}\|^{2}}_{\|d\overline{\boldsymbol{W}}_{t}\|^{2}} = (60)$$

$$= 1 - \eta_{\text{eff}}^2 \operatorname{Tr} \left( \mathbf{\Sigma}_{\overline{\boldsymbol{W}}_t} \right) dt + \eta_{\text{eff}}^2 \operatorname{Tr} \left( d\boldsymbol{B}_t^T \mathbf{\Sigma}_{\overline{\boldsymbol{W}}_t} d\boldsymbol{B}_t \right) = 1 - \eta_{\text{eff}}^2 \operatorname{Tr} \left( \mathbf{\Sigma}_{\overline{\boldsymbol{W}}_t} \right) dt + \eta_{\text{eff}}^2 \operatorname{Tr} \left( \mathbf{\Sigma}_{\overline{\boldsymbol{W}}_t} d\boldsymbol{B}_t d\boldsymbol{B}_t^T \right) =$$
(61)

$$= 1 - \eta_{\text{eff}}^2 \operatorname{Tr} \left( \mathbf{\Sigma}_{\overline{\mathbf{W}}_{\star}} \right) dt + \eta_{\text{eff}}^2 \operatorname{Tr} \left( \mathbf{\Sigma}_{\overline{\mathbf{W}}_{\star}} \mathbf{I}_d dt \right) = 1$$
 (62)

Here we substitute  $(dt)^2 = 0$ ,  $dt \cdot d(\mathbf{B}_t)_i = 0$ ,  $(d\mathbf{B}_t)_i^2 = dt$ , and  $(d\mathbf{B}_t)_i \cdot (d\mathbf{B}_t)_j = 0$  for  $i \neq j$ . Eq. 58 also describes the dynamics of the direction vector for the fixed sphere case.

Now, we analyze the solutions to these equations. If we have  $\operatorname{Tr}\Sigma_{\overline{w}}=\operatorname{const}$  for all  $\overline{w}$ , then the stationary radius  $r^*$  is given by

$$r^* = \sqrt{\frac{\eta_{\text{eff}}}{2\lambda} \operatorname{Tr} \Sigma_{\overline{\boldsymbol{w}}}}$$
 (63)

In the isotropic noise model, the covariance matrix trace reduces to

$$\operatorname{Tr} \Sigma_{\overline{\boldsymbol{w}}} = \operatorname{Tr} \left( \boldsymbol{P}_{\overline{\boldsymbol{w}}} (\sigma^2 \boldsymbol{I}_d) \boldsymbol{P}_{\overline{\boldsymbol{w}}} \right) = \sigma^2 \operatorname{Tr} \left( \boldsymbol{P}_{\overline{\boldsymbol{w}}} \boldsymbol{P}_{\overline{\boldsymbol{w}}} \right) = \sigma^2 \operatorname{Tr} \left( \boldsymbol{I}_d - \overline{\boldsymbol{w}} \, \overline{\boldsymbol{w}}^T \right) = \sigma^2 (d - 1)$$
 (64)

Thus we have

$$r^* = \sqrt{\frac{\eta_{\text{eff}}\sigma^2(d-1)}{2\lambda}} \tag{65}$$

Eq. 58 in the isotropic setting becomes

$$d\overline{\boldsymbol{W}}_{t} = -\left(\eta_{\text{eff}}\nabla L(\overline{\boldsymbol{W}}_{t}) + \frac{\eta_{\text{eff}}^{2}\sigma^{2}(d-1)}{2}\overline{\boldsymbol{W}}_{t}\right)dt + \eta_{\text{eff}}\sigma\boldsymbol{P}_{\overline{\boldsymbol{W}}_{t}}d\boldsymbol{B}_{t}$$
(66)

According to Wang and Wang (2022), the stationary distribution for this SDE is given by

$$\rho_{\overline{\boldsymbol{w}}}(\overline{\boldsymbol{w}}) \propto \exp\left(-\frac{L(\overline{\boldsymbol{w}})}{\tau_{\text{eff}}}\right), \quad \text{where } \tau_{\text{eff}} = \frac{\eta_{\text{eff}}\sigma^2}{2}$$
(67)

SGD with fixed LR The SGD iterates in the fixed LR case are

$$\boldsymbol{w}_{k+1} = \boldsymbol{w}_k - \eta \left( \nabla L_{\mathcal{B}_k}(\boldsymbol{w}_k) + \lambda \boldsymbol{w}_k \right) = \boldsymbol{w}_k - \eta \left( \nabla L(\boldsymbol{w}_k) + \lambda \boldsymbol{w}_k \right) - \eta \left( \boldsymbol{\Sigma}_{\boldsymbol{w}} \right)^{1/2} \boldsymbol{\varepsilon}, \tag{68}$$

where  $\varepsilon \sim \mathcal{N}(0, \mathbf{I}_d)$ . This discrete dynamics leads to the following SDE

$$d\mathbf{W}_{t} = -\eta \left(\nabla L(\mathbf{W}_{t}) + \lambda \mathbf{W}_{t}\right) dt + \eta \left(\mathbf{\Sigma}_{\mathbf{W}_{t}}\right)^{\frac{1}{2}} d\mathbf{B}_{t}$$
(69)

The derivation of the SDE for  $r_t$  and  $\overline{W}_t$  is analogous to the fixed ELR case. The only difference is that we need to divide the Ito's correction by  $r_t^4$  and the rest of terms by  $r_t^2$ . This gives the following equations

$$dr_t = \left(-\eta \lambda r_t + \frac{\eta^2}{2r_*^3} \operatorname{Tr} \mathbf{\Sigma}_{\overline{\mathbf{W}}_t}\right) dt \tag{70}$$

$$d\overline{\boldsymbol{W}}_{t} = -\left(\frac{\eta}{r_{t}^{2}}\nabla L(\overline{\boldsymbol{W}}_{t}) + \frac{\eta^{2}}{2r_{t}^{4}}\operatorname{Tr}\left(\boldsymbol{\Sigma}_{\overline{\boldsymbol{W}}_{t}}\right)\overline{\boldsymbol{W}}_{t}\right)dt + \frac{\eta}{r_{t}^{2}}\left(\boldsymbol{\Sigma}_{\overline{\boldsymbol{W}}_{t}}\right)^{\frac{1}{2}}d\boldsymbol{B}_{t}$$

$$(71)$$

The stationary radius for the **constant covariance trace** and in the **isotropic noise model**, respectively, is

$$r^* = \sqrt[4]{\frac{\eta_{\text{eff}}}{2\lambda} \operatorname{Tr} \Sigma_{\overline{w}}} = \sqrt[4]{\frac{\eta_{\text{eff}} \sigma^2 (d-1)}{2\lambda}}$$
 (72)

Eq. 71 in the isotropic case becomes

$$d\overline{\boldsymbol{W}}_{t} = -\left(\frac{\eta}{r_{t}^{2}}\nabla L(\overline{\boldsymbol{W}}_{t}) + \frac{\eta^{2}\sigma^{2}(d-1)}{2r_{t}^{4}}\overline{\boldsymbol{W}}_{t}\right)dt + \frac{\eta\sigma}{r_{t}^{2}}\boldsymbol{P}_{\overline{\boldsymbol{W}}_{t}}d\boldsymbol{B}_{t}$$

$$(73)$$

At stationary, we can replace  $r_t$  with  $r^*$ , so the resulting distribution of  $\overline{\boldsymbol{w}}$  is

$$\rho_{\overline{\boldsymbol{w}}}(\overline{\boldsymbol{w}}) \propto \exp\left(-\frac{L(\overline{\boldsymbol{w}})}{\tau/(r^*)^2}\right), \quad \text{where } \tau = \frac{\eta\sigma^2}{2}$$
(74)

#### D.2 First Law of Thermodynamics

In this section, we show that the First Law of Thermodynamics for reversible processes (i.e., where  $\delta Q = TdS$  is substituted) holds for stationary distributions of SGD, dU = TdS - pdV. Recall that

$$U = \mathbb{E}_{\rho_{\overline{w}}} \big[ L(\overline{w}) \big], \qquad S = \mathbb{E}_{\rho_{\overline{w}}} \big[ -\log \rho_{\overline{w}}(\overline{w}) \big] + \frac{d-1}{2} \log(2V), \qquad \rho_{\overline{w}}(\overline{w}) = \frac{1}{Z(T)} \exp\left( -\frac{L(\overline{w})}{T} \right), \tag{75}$$

where Z(T) denotes the normalization constant. We can represent S as

$$S = \mathbb{E}_{\rho_{\overline{w}}} \left[ \log Z(T) + \frac{L(\overline{w})}{T} \right] + \frac{d-1}{2} \log(2V) = \frac{U}{T} + \log Z(T) + \frac{d-1}{2} \log(2V)$$
 (76)

Taking the differential, we obtain

$$dS = \frac{1}{T}dU - \frac{U}{T^2}dT + \frac{Z'(T)}{Z(T)}dT + \frac{d-1}{2V}dV$$
(77)

Now, we show that  $\frac{U}{T^2} = \frac{Z'(T)}{Z(T)}$ 

$$\frac{Z'(T)}{Z(T)} = \frac{1}{Z(T)} \cdot \frac{\mathrm{d}}{\mathrm{d}T} \int_{\mathbb{S}^{d-1}} \exp\left(-\frac{L(\overline{\boldsymbol{w}})}{T}\right) d\overline{\boldsymbol{w}} = \frac{1}{Z(T)} \cdot \int_{\mathbb{S}^{d-1}} \frac{\mathrm{d}}{\mathrm{d}T} \exp\left(-\frac{L(\overline{\boldsymbol{w}})}{T}\right) d\overline{\boldsymbol{w}} = 
= \frac{1}{Z(T)} \cdot \int_{\mathbb{S}^{d-1}} \exp\left(-\frac{L(\overline{\boldsymbol{w}})}{T}\right) \frac{L(\overline{\boldsymbol{w}})}{T^2} d\overline{\boldsymbol{w}} = \frac{1}{T^2} \cdot \int_{\mathbb{S}^{d-1}} \frac{L(\overline{\boldsymbol{w}})}{Z(T)} \exp\left(-\frac{L(\overline{\boldsymbol{w}})}{T}\right) d\overline{\boldsymbol{w}} = \frac{U}{T^2}$$
(78)

Thus,  $dS = \frac{1}{T}dU + \frac{d-1}{2V}dV$ . Hence

$$TdS - pdV = dU + \underbrace{\frac{T(d-1)}{2V}}_{p} dV - pdV = dU$$

$$\tag{79}$$

Note that we used the stationary distribution on the unit sphere and the ideal gas law  $p = \frac{T(d-1)}{2V}$  (i.e., the stationary radius expression) to derive this relation.

Once the First Law is established, we can also derive the expression for Helmholtz and Gibbs energies. The key idea is that these potentials should be total differentials in the corresponding natural variables: T, V for F and T, p for G. This is done via so-called Legendre transformation

$$F = U - \frac{\partial U}{\partial S}S = U - TS, \qquad dF = dU - d(TS) = TdS - pdV - TdS - SdT = -SdT - pdV$$
(80)

$$G = F - \frac{\partial F}{\partial V}V = F + pV, \qquad dG = dF + d(pV) = -SdT - pdV + pdV + Vdp = -SdT + Vdp \tag{81}$$

#### D.3 Maxwell relations

In this section, we derive specific Maxwell relations for three considered training protocols.

**SGD** on a fixed sphere For the fixed sphere case, verifying the Maxwell relation is equivalent to checking that the pressure follows the ideal gas law  $p = \frac{T(d-1)}{2V}$ 

$$\left(\frac{\partial p}{\partial T}\right)_{V} = \left(\frac{\partial S}{\partial V}\right)_{T} = \frac{d-1}{2V} \tag{82}$$

Although there is no explicit application of weight decay in this training protocol, we can estimate the effective weight decay  $\lambda_{\text{eff}}$ , which is associated with the projection back to the sphere  $\mathbb{S}^{d-1}(r)$  after each training step. In other words, it is the value of the weight decay coefficient required to maintain the dynamics on the same sphere, which we estimate empirically as

$$\lambda_{\text{eff}} = \mathbb{E}\left[\frac{\|\boldsymbol{w}_k - \eta \nabla L_{\mathcal{B}_k}(\boldsymbol{w}_k)\| - \|\boldsymbol{w}_k\|}{\eta \|\boldsymbol{w}_k\|}\right],\tag{83}$$

where  $\eta = \eta_{\text{eff}} \|\boldsymbol{w}_k\|^2$  and  $\|\boldsymbol{w}_k\| = r$ . Similarly to the fixed ELR/LR cases, we interpret the effective weight decay  $\lambda_{\text{eff}}$  as pressure p. Thus, verifying both the Maxwell relation and the ideal gas law reduces to checking whether

$$\lambda_{\text{eff}} = \frac{T(d-1)}{2V} = \frac{\eta_{\text{eff}}\sigma^2(d-1)}{2r^2}$$
(84)

**SGD with fixed ELR** Training protocol for SGD with fixed ELR corresponds to fixing T and p with the Maxwell relation  $-\left(\frac{\partial S}{\partial p}\right)_T = \left(\frac{\partial V}{\partial T}\right)_p$ . Considering  $V = \frac{T(d-1)}{2p}$ , we get  $\left(\frac{\partial V}{\partial T}\right)_p = \frac{d-1}{2p}$ . Finally, given  $\left(\frac{\partial S}{\partial p}\right)_T = \frac{1}{p}\left(\frac{\partial S}{\partial \log p}\right)_T$  and substituting  $p = \lambda$ , we get (note that fixing T corresponds to fixing  $\eta_{\text{eff}}$ )

$$\left(\frac{\partial S}{\partial \log \lambda}\right)_{\eta_{\text{eff}}} = -\frac{d-1}{2} \tag{85}$$

**SGD** with fixed LR In the fixed LR case, T is dependent on both  $\eta$  and  $\lambda$ , so we introduce this pair as new natural variables (instead of T and p). We also consider  $\sigma = \sigma(\eta\lambda)$  to account for variable variance in the experiments, as shown in Subfigure 2a. Despite  $\sigma$  being variable, we obtain the same Eq. 23. To start with, we express the differential of  $T = \sqrt{\frac{\eta\lambda\sigma^2(\eta\lambda)}{2(d-1)}}$  (for brevity, we omit the brackets in  $\sigma(\eta\lambda)$  and  $\sigma'(\eta\lambda)$ )

$$\left(\frac{\partial T}{\partial \eta}\right)_{\lambda} = \sqrt{\frac{\lambda \sigma^2}{2(d-1)}} \cdot \frac{1}{2\sqrt{\eta}} + \sqrt{\frac{\eta \lambda}{2(d-1)}} \cdot \sigma' \lambda = \sqrt{\frac{\eta \lambda}{2(d-1)}} \left(\frac{\sigma}{2\eta} + \sigma' \lambda\right) \tag{86}$$

$$\left(\frac{\partial T}{\partial \lambda}\right)_{\eta} = \sqrt{\frac{\eta \sigma^2}{2(d-1)}} \cdot \frac{1}{2\sqrt{\lambda}} + \sqrt{\frac{\eta \lambda}{2(d-1)}} \cdot \sigma' \eta = \sqrt{\frac{\eta \lambda}{2(d-1)}} \left(\frac{\sigma}{2\lambda} + \sigma' \eta\right) \tag{87}$$

$$dT = \left(\frac{\partial T}{\partial \eta}\right)_{\lambda} d\eta + \left(\frac{\partial T}{\partial \lambda}\right)_{\eta} d\lambda \tag{88}$$

Thus, the differential of Gibbs energy (Eq. 81) is

$$dG = -SdT + Vdp = -S\left(\frac{\partial T}{\partial \eta}\right)_{\lambda} d\eta - S\left(\frac{\partial T}{\partial \lambda}\right)_{\eta} d\lambda + Vd\lambda = -S\left(\frac{\partial T}{\partial \eta}\right)_{\lambda} d\eta + \left[V - S\left(\frac{\partial T}{\partial \lambda}\right)_{\eta}\right] d\lambda \tag{89}$$

To derive the Maxwell relation, we need to equate the second cross-derivatives

$$-\frac{\partial}{\partial \lambda} \left[ S \left( \frac{\partial T}{\partial \eta} \right)_{\lambda} \right] = \frac{\partial}{\partial \eta} \left[ V - S \left( \frac{\partial T}{\partial \lambda} \right)_{\eta} \right] \tag{90}$$

$$-\left(\frac{\partial S}{\partial \lambda}\right)_{\eta}\left(\frac{\partial T}{\partial \eta}\right)_{\lambda} - S\left(\frac{\partial^{2} T}{\partial \eta \partial \lambda}\right) = \left(\frac{\partial V}{\partial \eta}\right)_{\lambda} - \left(\frac{\partial S}{\partial \eta}\right)_{\lambda}\left(\frac{\partial T}{\partial \lambda}\right)_{\eta} - S\left(\frac{\partial^{2} T}{\partial \eta \partial \lambda}\right) \tag{91}$$

$$-\left(\frac{\partial S}{\partial \lambda}\right)_{\eta} \left(\frac{\partial T}{\partial \eta}\right)_{\lambda} = \left(\frac{\partial V}{\partial T}\right)_{\lambda} \left(\frac{\partial T}{\partial \eta}\right)_{\lambda} - \left(\frac{\partial S}{\partial \eta}\right)_{\lambda} \left(\frac{\partial T}{\partial \lambda}\right)_{\eta} \tag{92}$$

$$-\left(\frac{\partial S}{\partial \lambda}\right)_{\eta} \sqrt{\frac{\eta \chi}{2(d-1)}} \left(\frac{\sigma}{2\eta} + \sigma' \lambda\right) = \frac{d-1}{2\lambda} \sqrt{\frac{\eta \chi}{2(d-1)}} \left(\frac{\sigma}{2\eta} + \sigma' \lambda\right) - \left(\frac{\partial S}{\partial \eta}\right)_{\lambda} \sqrt{\frac{\eta \chi}{2(d-1)}} \left(\frac{\sigma}{2\lambda} + \sigma' \eta\right) \tag{93}$$

$$-\frac{1}{\lambda} \left( \frac{\partial S}{\partial \log \lambda} \right)_{\eta} \left( \frac{\sigma}{2\eta} + \sigma' \lambda \right) = \frac{d-1}{2\lambda} \left( \frac{\sigma}{2\eta} + \sigma' \lambda \right) - \frac{1}{\eta} \left( \frac{\partial S}{\partial \log \eta} \right)_{\lambda} \left( \frac{\sigma}{2\lambda} + \sigma' \eta \right) \tag{94}$$

$$-\left(\frac{\partial S}{\partial \log \lambda}\right)_{\eta} \left(\frac{\sigma}{2\eta\lambda} + \sigma'\right) = \frac{d-1}{2} \left(\frac{\sigma}{2\eta\lambda} + \sigma'\right) - \left(\frac{\partial S}{\partial \log \eta}\right)_{\lambda} \left(\frac{\sigma}{2\eta\lambda} + \sigma'\right) \tag{95}$$

$$\left(\frac{\partial S}{\partial \log \eta}\right)_{\lambda} - \left(\frac{\partial S}{\partial \log \lambda}\right)_{\eta} = \frac{d-1}{2} \tag{96}$$

All terms including  $\sigma$  and  $\sigma'$  are eliminated, so the formula holds for both constant and variable  $\sigma$ .

#### D.4 Heat capacity and adiabatic constant

In this section, we derive the relation for heat capacities  $C_p - C_V = R$  in our analogy and show that the adiabatic process is given by  $pV^{\gamma} = \text{const}$  with  $\gamma = C_p/C_V$ . We use the expressions  $\delta Q = \mathrm{d}U + p\mathrm{d}V$ ,  $V = \frac{T(d-1)}{2p}$ , and the fact that U is a function of temperature T

$$C_{V} = \left(\frac{\delta Q}{\mathrm{d}T}\right)_{V} = \left(\frac{\partial U}{\partial T}\right)_{V} = \frac{\mathrm{d}U}{\mathrm{d}T}, \qquad C_{p} = \left(\frac{\delta Q}{\mathrm{d}T}\right)_{p} = \left(\frac{\partial U}{\partial T}\right)_{p} + p\left(\frac{\partial V}{\partial T}\right)_{p} = \frac{\mathrm{d}U}{\mathrm{d}T} + p\frac{d-1}{2p} = C_{V} + R \qquad (97)$$

Now, we set  $\delta Q = 0$  and relate dp and dV

$$0 = \delta Q = dU + pdV = C_V dT + pdV = C_V d\left(\frac{PV}{R}\right) + pdV =$$

$$= \frac{C_V}{R} \left(pdV + Vdp\right) + pdV = \frac{C_p}{R} pdV + \frac{C_V}{R} Vdp$$
(98)

$$C_V V dp = -C_p p dV \Leftrightarrow \frac{dp}{p} = -\gamma \frac{dV}{V} \Leftrightarrow \log p = -\gamma \log V + \text{const} \Leftrightarrow \log(pV^{\gamma}) = \text{const} \Leftrightarrow pV^{\gamma} = \text{const}$$

$$(99)$$

#### D.5 Spherical entropy estimator

In this section, we proof the Eq. 26, which relates entropy on the unit sphere  $S_{\mathbb{S}^{d-1}}(\overline{\boldsymbol{w}})$  and angular entropy  $S_{\mathbb{R}^{d-1}}(\boldsymbol{\theta})$ . Under the change of variables, the densities are related as  $\rho_{\boldsymbol{\theta}}(\boldsymbol{\theta}) = \rho_{\overline{\boldsymbol{w}}}(\overline{\boldsymbol{w}})J(\boldsymbol{\theta})$ . Hence

$$S_{\mathbb{S}^{d-1}}(\overline{\boldsymbol{w}}) = \mathbb{E}_{\rho_{\overline{\boldsymbol{w}}}} \left[ -\log \rho_{\overline{\boldsymbol{w}}}(\overline{\boldsymbol{w}}) \right] = \mathbb{E}_{\rho_{\overline{\boldsymbol{w}}}} \left[ -\log \rho_{\boldsymbol{\theta}}(\boldsymbol{\theta}) + \log J(\boldsymbol{\theta}) \right] = S_{\mathbb{R}^{d-1}}(\boldsymbol{\theta}) + \mathbb{E}_{\rho_{\overline{\boldsymbol{w}}}} \left[ \log J(\boldsymbol{\theta}) \right]$$
(100)

The constant C(N,d) in the entropy estimator (Eq. 25) is

$$C(N,d) = \log(N-1) - \log\Gamma\left(\frac{d}{2} + 1\right) + \frac{d}{2}\log\pi + \gamma,\tag{101}$$

where  $\Gamma$  denotes the gamma function, and  $\gamma \approx 0.577$  is the Euler constant.

#### E ADDITIONAL RESULTS FOR ISOTROPIC NOISE MODEL

Statistics of VMF distribution For consistency with the existing sources, we derive the statistics of the VMF distribution for inverse temperature  $\kappa = 1/T$  and then we rewrite them in terms of the original temperature T. The density is given by<sup>4</sup>

$$\rho_{\overline{\boldsymbol{w}}}(\overline{\boldsymbol{w}}) = C_d(\kappa) \exp\left(-\kappa \boldsymbol{\mu}^T \overline{\boldsymbol{w}}\right), \quad \text{where } C_d(\kappa) = \frac{\kappa^{d/2 - 1}}{(2\pi)^{d/2} I_{d/2 - 1}(\kappa)}, \quad (102)$$

where  $I_{d/2-1}(\kappa)$  is the modified Bessel function of first kind. The expected loss U and entropy S for this distribution are

$$U = \mathbb{E}_{\rho_{\overline{w}}} \left[ 1 + \boldsymbol{\mu}^T \overline{\boldsymbol{w}} \right] = 1 - \boldsymbol{\mu}^T A_d(\kappa) \boldsymbol{\mu} = 1 - A_d(\kappa) \quad S = -\log C_d(\kappa) - \kappa A_d(\kappa), \quad \text{with } A_d(\kappa) = \frac{I_{d/2}(\kappa)}{I_{d/2-1}(\kappa)}$$
(103)

We are interested in the asymptotics of these functions in the limit  $\kappa \to \infty$  (i.e.,  $T \to 0$ , so that we can apply this approximation for sufficiently small values of  $\eta$  and  $\lambda$ ). Olver et al. (2025) give the following approximation for  $I_{\nu}(\kappa)$  in 10.40.1

$$I_{\nu}(\kappa) = \frac{e^{\kappa}}{\sqrt{2\pi\kappa}} \left( 1 - \frac{4\nu^2 - 1}{8\kappa} + \overline{o}(\kappa^{-1}) \right)$$
 (104)

Let  $\nu = d/2$ . The asymptotics for  $A_d(\kappa)$  is

$$A_{d}(\kappa) = \frac{I_{\nu}(\kappa)}{I_{\nu-1}(\kappa)} = \frac{1 - \frac{4\nu^{2} - 1}{8\kappa} + \overline{o}(\kappa^{-1})}{1 - \frac{4(\nu-1)^{2} - 1}{8\kappa} + \overline{o}(\kappa^{-1})} = 1 - \frac{(4\nu^{2} - 1) - (4(\nu-1)^{2} - 1)}{8\kappa} + \overline{o}(\kappa^{-1}) = 1 - \frac{8\nu - 4}{8\kappa} + \overline{o}(\kappa^{-1}) = 1 - \frac{2\nu - 1}{2\kappa} + \overline{o}(\kappa^{-1}) = 1 - \frac{d - 1}{2\kappa} + \overline{o}(\kappa^{-1})$$

$$(105)$$

Thus, the expected loss U is:

$$U = 1 - A_d(\kappa) = \frac{d-1}{2\kappa} + \bar{o}(\kappa^{-1}) = \frac{d-1}{2}T + \bar{o}(T)$$
 (106)

The entropy S is

$$S = -\log C_d(\kappa) - \kappa A_d(\kappa) = -\left(\frac{d}{2} - 1\right) \log \kappa + \frac{d}{2} \log(2\pi) + \log\left(\frac{e^{\kappa}}{\sqrt{2\pi\kappa}} \left(1 - \frac{4(d/2 - 1)^2 - 1}{8\kappa} + \overline{o}(\kappa^{-1})\right)\right) - \kappa \left(1 - \frac{d - 1}{2\kappa} + \overline{o}(\kappa^{-1})\right) = -\left(\frac{d}{2} - 1\right) \log \kappa + \frac{d}{2} \log(2\pi) + \kappa - \frac{1}{2} \log(2\pi) - \frac{1}{2} \log \kappa - \kappa + \frac{d - 1}{2} + \overline{o}(1) = \frac{d - 1}{2} \log\left(\frac{2\pi e}{\kappa}\right) + \overline{o}(1) = \frac{d - 1}{2} \log\left(2\pi e^{\kappa}\right) + \overline{o}(1)$$

$$(107)$$

<sup>&</sup>lt;sup>4</sup>https://en.wikipedia.org/wiki/Von\_Mises-Fisher\_distribution

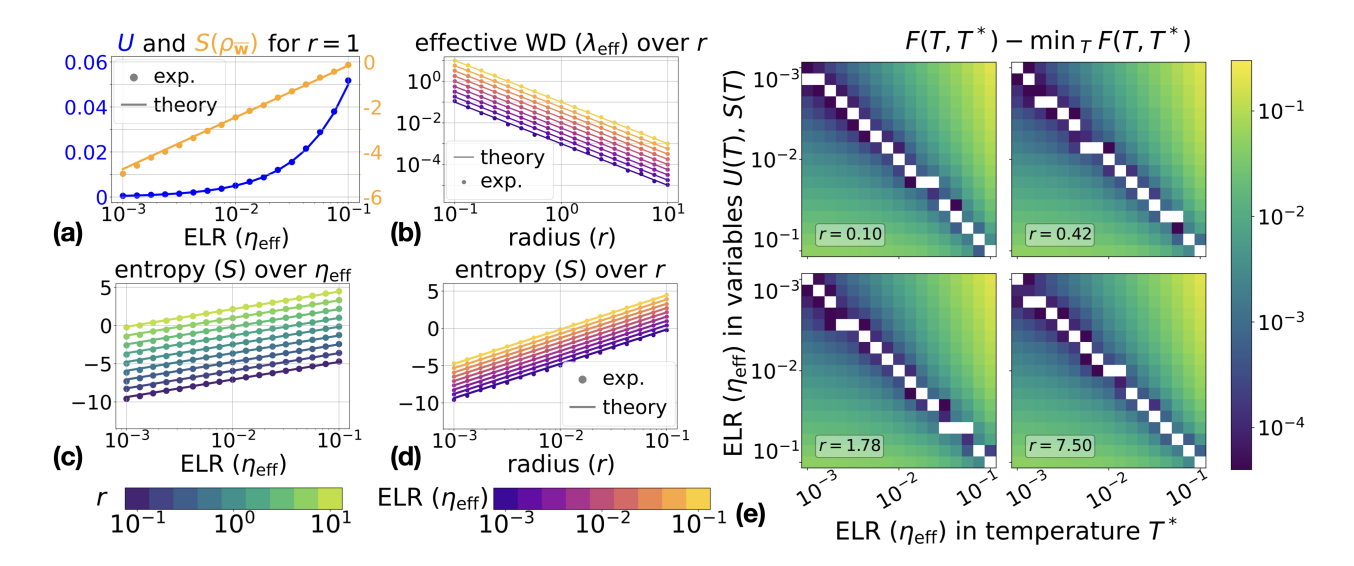


Figure 3: Results for the VMF isotropic noise model on a fixed sphere with radius r and ELR  $\eta_{\rm eff}$ . Subfigures a–d: points are numerical measurements, solid lines are theoretical predictions:  $U = \frac{d-1}{2}T$ ,  $S(\rho_{\overline{w}}) = \frac{d-1}{2}\log(2\pi eT)$ ,  $S = S(\rho_{\overline{w}}) + (d-1)\log r$ , and  $\lambda_{\rm eff} = \frac{T(d-1)}{2V}$ , with  $T = \frac{\eta_{\rm eff}\sigma^2}{2}$  and  $V = \frac{r^2}{2}$ . Subfigure e: Helmholtz energy minimization (V2). Each subplot corresponds to a radius value r. On the horizontal axis, we vary  $\eta_{\rm eff}$  in temperature  $T^*$  of Helmholtz energy F; on the vertical axis, we consider stationary distributions induced by different  $\eta_{\rm eff}$ . The colormap shows the difference between F and its minimum across different stationary distributions (i.e., across each column), with the minimizer marked by a white square. Ideally, white squares coincide with the diagonal; in practice, they either match or lie very close.

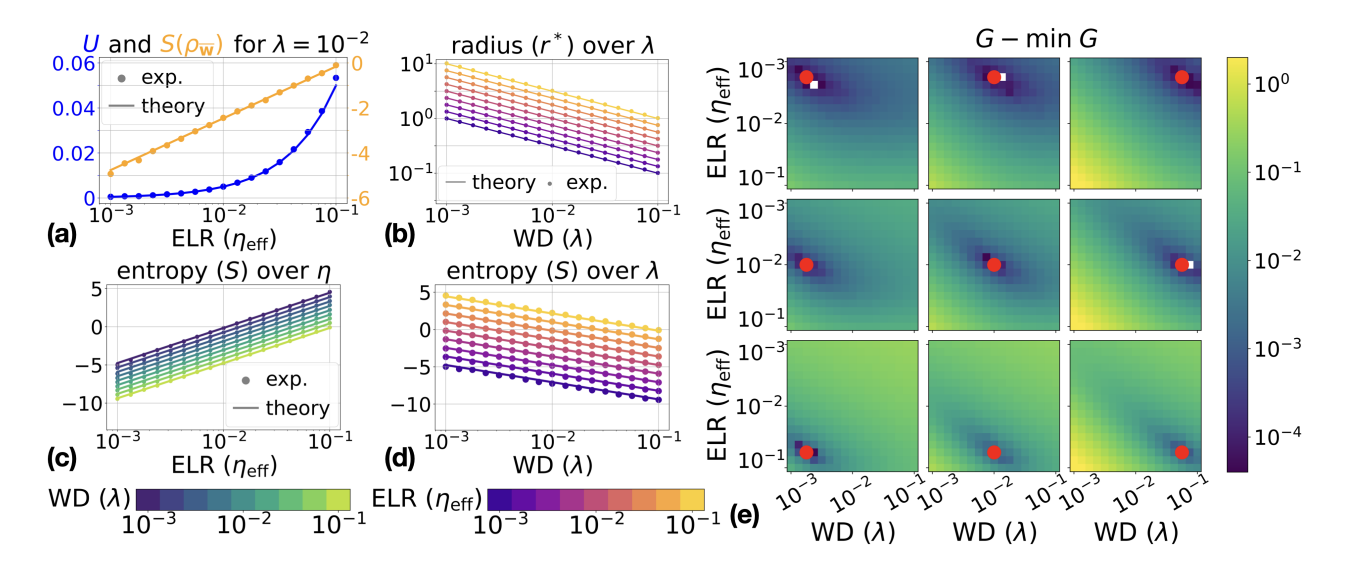


Figure 4: Results for the VMF isotropic noise model with fixed ELR  $\eta_{\rm eff}$  and WD  $\lambda$ . Subfigures a–d: points are numerical measurements, solid lines are theoretical predictions:  $U = \frac{d-1}{2}T$ ,  $S(\rho_{\overline{w}}) = \frac{d-1}{2}\log(2\pi eT)$ ,  $S = S(\rho_{\overline{w}}) + (d-1)\log r^*$ , and  $r^* = \sqrt{\frac{T(d-1)}{p}}$ , with  $T = \frac{\eta_{\rm eff}\sigma^2}{2}$  and  $p = \lambda$ . Subfigure e: Gibbs energy minimization (V2). Each subplot corresponds to a fixed pair  $(\eta_{\rm eff}^*, \lambda^*)$ , denoted with red circle. The colormap shows the difference between G and its minimum across stationary distributions, with the minimizer marked by a white square. Ideally, red circles coincide with white squares; in practice, they either match or lie very close.

Training setup	ResNet-18 CIFAR-10	ResNet-18 CIFAR-100	ConvNet CIFAR-10	ConvNet CIFAR-100
*1/1 1: 1: / /				
width multipliet $k$	4	4	8	16
number of trainable parameters $d$	43692	43692	24408	97200
training iterations $t$	$10^{6}$	$2 \cdot 10^6$	$2 \cdot 10^{6}$	$2 \cdot 10^{6}$
entropy queue size $N$	1000	1000	4000	4000
ELR grid $\eta_{\rm eff}$	$\{10^{-4+n/6} n$	$a = 0, \dots, 13$	$\{10^{-4+n}$	$\frac{1}{2^{6} n=0,\dots,12}$
LR grid $\eta$		$a=0,\ldots,18$	$\{10^{-3+n}$	$n^{1/6} n=0,\ldots,12\}$
WD grid $\lambda$	$\{10^{-3+n/2} n$	$n=0,\ldots,4$	$\{10^{-3+n/4} \text{ and }$	$10^{-2+n/4}   n = 0, \dots, 8 $
radius grid $r$		${2^{-2}}$	$+^n n=0,\ldots,4\}$	

Table 3: Differences across configurations among the training setups. In the WD grid for ConvNet,  $10^{-3+n/4}$  and  $10^{-2+n/4}$  correspond to CIFAR-10 and CIFAR-100, respectively. We consider higher LR values compared to ELR values to maintain similar temperature ranges. For the same reason we adopt higher WD values for ConvNet CIFAR-100 experiment.

Detailed experimental setup We launch noisy gradient descent given by Eq. 24 for  $2 \cdot 10^6$  iterations. The gradient variance is set to  $\sigma = 1$ . We consider  $\eta, \eta_{\text{eff}}, \lambda \in [10^{-3}, 10^{-1}]$ . In the case of the fixed sphere, we sweep over  $r \in [10^{-1}, 10^1]$ . We sample  $\mu$  from the uniform distribution on  $\mathbb{S}^{d-1}$  and keep it the same for all the considered hyperparameter values. For all of these ranges, we take 17 values equally spaced in the logarithmic domain. We log training loss and radius every 50 iterations. To calculate the mean values for stationary distributions, we average over last 5000 logs. Entropy is logged every 40000 iterations. The stationary entropy is the average of the last 10 logs. The isotropic noise model is implemented on CPU; running one training protocol for a square grid of hyperparameters requires < 10 minutes.

Results for VMF model In Figure 3, we present the results of numerical simulation for training on a fixed sphere. Similarly to the fixed LR case, empirical U and  $S(\rho_{\overline{w}})$  closely follow their theoretic predictions in Subfigure 3a, confirming that the stationary distribution is of the VMF form. The minimization of Helmholtz energy in Subfigure 3e proves V2. Subfigure 3b verifies V3, which is equivalent to checking the stationary pressure (i.e., the effective weight decay, Eq. 82). Similarly, Figure 4 demonstrates the case of training with the fixed ELR. All empirical quantities meet the corresponding theoretic predictions, and the Gibbs energy G is minimized among the considered stationary distributions.

#### F ADDITIONAL RESULTS FOR NEURAL NETWORKS

Detailed experimental setup We train two architectures—ResNet-18 (He et al., 2016) and a ConvNet with four convolutional layers (adapted from Kodryan et al. (2022))—on the CIFAR-10 (Krizhevsky et al., 2009a) and CIFAR-100 (Krizhevsky et al., 2009b) datasets. Both models are made fully scale-invariant by inserting a BatchNorm layer without affine parameters after each convolutional layer. The final linear layer is kept fixed with its weight norm set to 10. In both the fixed ELR and fixed LR training protocols, the initial norm of trainable parameters is set to  $\|\boldsymbol{w}_0\| = 1$ . We use a batch size of B = 128 across all experiments, sampling batches independently at each iteration, thus, there is no notion of epochs.

We apply no data augmentations other than channel-wise normalization. For CIFAR-10, we use mean (0.4914, 0.4822, 0.4465) and standard deviation (0.2023, 0.1994, 0.2010); for CIFAR-100, we use mean (0.5071, 0.4867, 0.4408) and standard deviation (0.2675, 0.2565, 0.2761). New weights are added to the entropy estimation queue every 25 iterations. All other hyperparameters that differ across training setups, including grids for  $\eta_{\text{eff}}$ ,  $\eta$ ,  $\lambda$ , and r, are listed in Table 3. We record metrics every 200 iterations during the first 10,000 iterations of training (corresponding to 50 logs). The remaining 150 logs are sampled at logarithmically spaced intervals until the end of training. For stationary metrics, we report averages computed over the last 30 logs.

The code for reproducing all experiments is available at https://github.com/isadrtdinov/neural-nets-ideal-gas.

Tra	ining setup	ResNet-18 CIFAR-10	ResNet-18 CIFAR-100	ConvNet CIFAR-10	ConvNet CIFAR-100
	approximation $\mathbb{R}^2$	0.9926	0.9949	0.9975	0.9791
	$a_2/(\frac{d-1}{2})$	-1.029	-1.022	-1.128	-0.930
Fixed ELR	$2a_4/(\frac{d-1}{2})$	-0.008	-0.006	-0.016	-0.0015
	$a_5/(\frac{d-1}{2})$	0.0002	0.0005	-0.006	0.009
	max. relative error	2.5%	1.9%	6.5%	4.0%
	approximation $\mathbb{R}^2$	0.9939	0.9894	0.9926	0.8412
Fixed LR	$(a_1 - a_2)/(\frac{d-1}{2})$	0.993	1.075	0.989	0.659
	$(2a_3 - a_5)/(\frac{d-1}{2})$	0.005	0.00008	-0.038	-0.047
	$(2a_4 - a_5)/(\frac{d-1}{2})$	0.005	-0.008	-0.033	0.0007
	max. relative error	3.0%	5.6%	17.6%	23.3%

Table 4: Verification of Maxwell relation for quadratic approximation of entropy.

Computational resources All experiments are conducted on NVIDIA A100 and H100 GPUs. Depending on the architecture and GPU type, individual training runs range from approximately 2–3 hours (for the ConvNet on CIFAR-10) to 6–9 hours (for the overparameterized ResNet-18, described in Appendix H). The total computational cost amounts to roughly 6,000 GPU hours.

Results The results, complementing Figure 2 from the main text, are presented in Figures 5, 6, 7, 8, 9, 10. These cover all four architecture-dataset pairs and three training protocols. Overall, these experiments confirm the results presented in the main text. First, the variance of stochastic gradients  $\sigma$  depends solely on  $\eta_{\rm eff}$  (in the fixed ELR and fixed sphere settings) and on the product  $\eta\lambda$  (in the fixed LR setting). Second, the temperature T generally increases with  $\eta$  or  $\eta_{\rm eff}$ , except at the largest values, where non-monotonic behavior is observed. Specifically, T first decreases, due to deviations of  $\sigma^2$  from its general trend, and then increases again (Figures 5b, 6b) in setups that explore higher ranges of hyperparameters. Sadrtdinov et al. (2024) demonstrate that for relatively large LRs (so-called regime 2B), the properties of the loss landscape in the region where the network settles change substantially, affecting both generalization and sharpness metrics. This phenomenon may explain the non-trivial dependencies observed in  $\sigma^2$  and T. Finally, the experimental values of the stationary radius  $r^*$  and effective weight decay  $\lambda_{\rm eff}$  closely match their theoretical predictions.

To verify the Maxwell relations  ${f V3}$ , we smooth the entropy values using polynomial regression up to quadratic terms.<sup>5</sup>

$$S(\log \eta, \log \lambda) = a_0 + a_1 \log \eta + a_2 \log \lambda + a_3 \log^2 \eta + a_4 \log^2 \lambda + a_5 \log \eta \log \lambda, \tag{108}$$

The resulting partial derivatives are

$$\left(\frac{\partial S}{\partial \log \eta}\right)_{\lambda} = a_1 + 2a_3 \log \eta + a_5 \log \lambda \qquad \left(\frac{\partial S}{\partial \log \lambda}\right)_{\eta} = a_2 + 2a_4 \log \lambda + a_5 \log \eta \tag{109}$$

In the fixed ELR case, we need to check that  $\left(\frac{\partial S}{\partial \log \lambda}\right)_{\eta_{\text{eff}}} = -\frac{d-1}{2}$ , which is equivalent to  $a_2 = -\frac{d-1}{2}$ ,  $2a_4 = 0$ , and  $a_5 = 0$ . We report the coefficients divided by  $\frac{d-1}{2}$  to evaluate their relative contribution to the derivative, i.e., we should get  $\frac{a_2}{(d-1)/2} \approx -1$ ,  $\frac{2a_4}{(d-1)/2} \approx 0$ , and  $\frac{a_5}{(d-1)/2} \approx 0$ .

In the fixed LR case, the Maxwell relation is

$$\left(\frac{\partial S}{\partial \log \eta}\right)_{\lambda} - \left(\frac{\partial S}{\partial \log \lambda}\right)_{\eta} = \frac{d-1}{2},\tag{110}$$

which is equivalent to  $a_1-a_2=\frac{d-1}{2},\ 2a_3-a_5=0,\ \text{and}\ 2a_4-a_5=0$  (we check that  $\frac{a_1-a_2}{(d-1)/2}\approx 1,\ \frac{2a_3-a_5}{(d-1)/2}\approx 0,$  and  $\frac{2a_4-a_5}{(d-1)/2}\approx 0$ ). The results of the numerical verification are summarized in Table 4. For most training

<sup>&</sup>lt;sup>5</sup>In the fixed ELR case, we similarly approximate the entropy as a function of  $\log \eta_{\rm eff}$  and  $\log \lambda$ .

setups, the maximum relative error remains low (below 10%). Two notable exceptions occur in the ConvNet experiments on CIFAR-10 and CIFAR-100 with a fixed LR, where the discrepancies increase to 17.6% and 23.3%, respectively. These higher errors appear near the boundaries of the hyperparameter ranges; when considering the average rather than the maximum error, the values drop to 6.1% and 12.3%, indicating that the approximation is substantially more accurate in the interior of the ranges, where entropy is estimated more reliably. The larger error in the CIFAR-100 setting is also explained by the highly noisy entropy values observed in Figure 6, which result in a lower coefficient of determination ( $R^2 \approx 0.84$ ) and a less reliable entropy approximation.

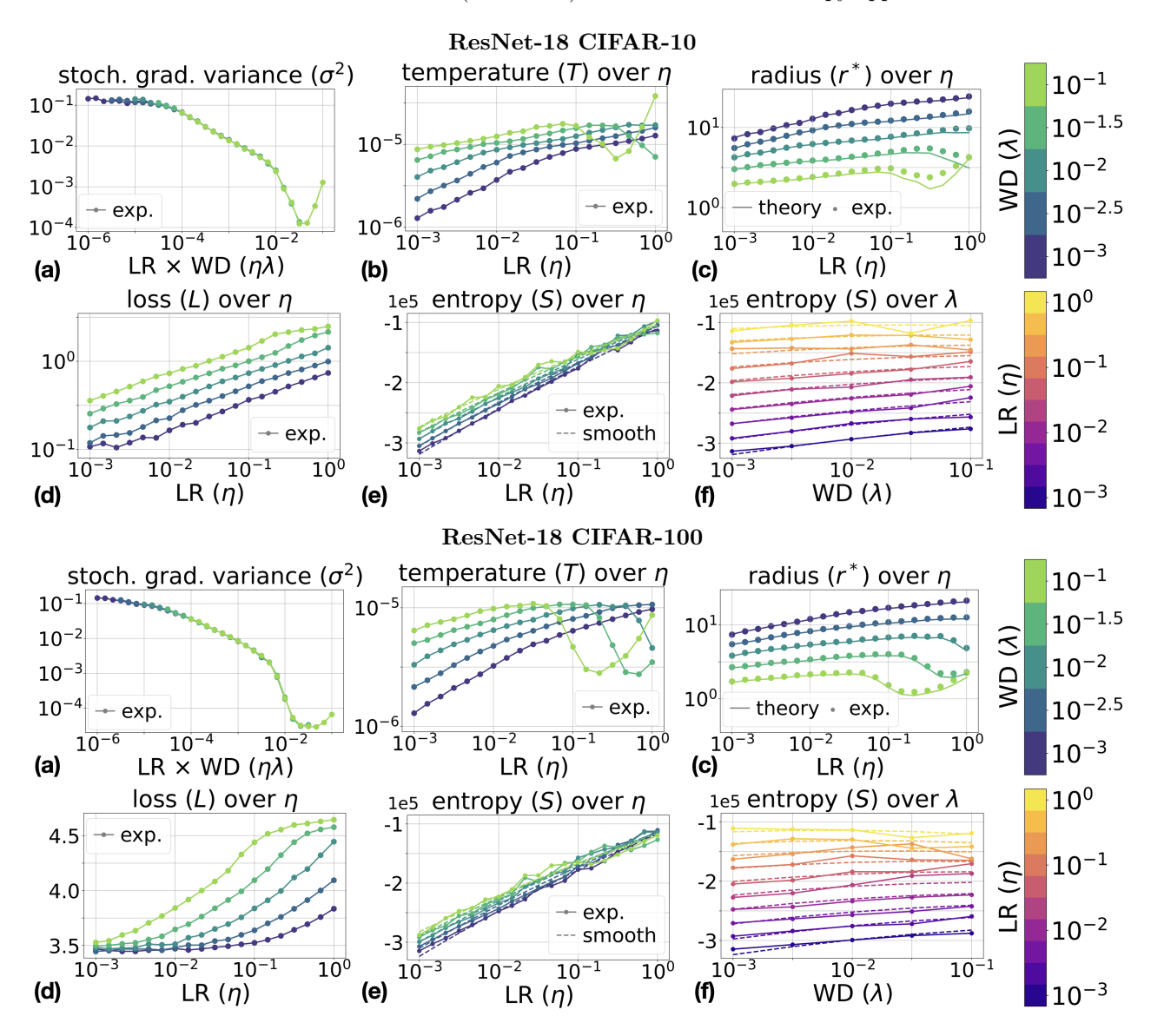


Figure 5: Results for ResNet-18 on CIFAR-10 and CIFAR-100 with fixed LR  $\eta$  and WD  $\lambda$ . Subfigures a, b, d: empirically measured  $\sigma^2$ , mean loss L, and temperature T given by  $T = \sqrt{\frac{\eta \lambda \sigma^2}{2(d-1)}}$ , respectively. Subfigure c: stationary radius  $r^* = \sqrt{\frac{T(d-1)}{p}}$  (solid lines, theory) vs. experimental values (points). Subfigures e and f: entropy S as a function of  $\eta$  and  $\lambda$ ; solid lines with markers show experimental estimates, dashed lines their smoothed versions.

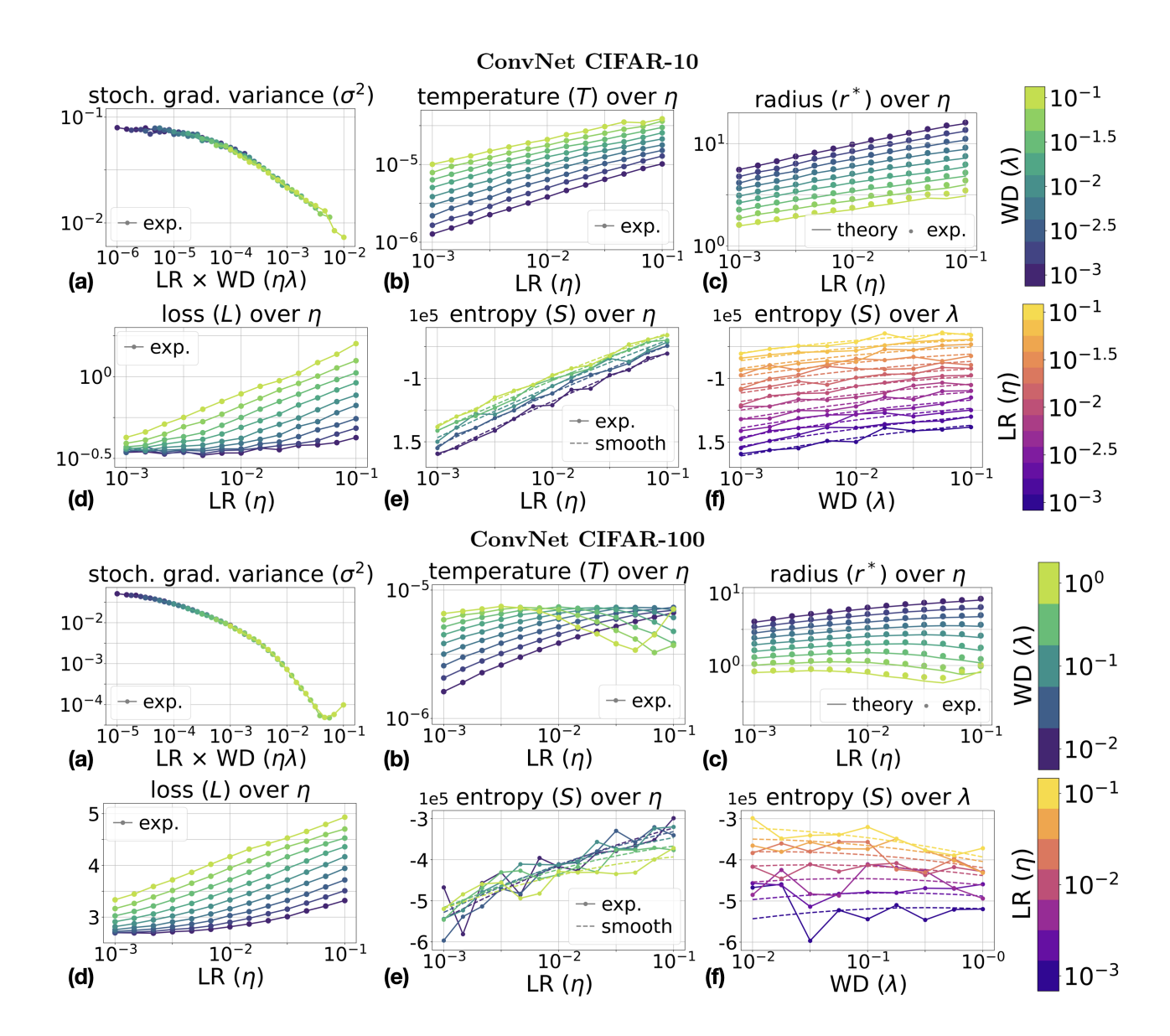


Figure 6: Results for ConvNet on CIFAR-10 and CIFAR-100 with fixed LR  $\eta$  and WD  $\lambda$ . Subfigures a, b, d: empirically measured  $\sigma^2$ , mean loss L, and temperature T given by  $T = \sqrt{\frac{\eta \lambda \sigma^2}{2(d-1)}}$ , respectively. Subfigure c: stationary radius  $r^* = \sqrt{\frac{T(d-1)}{p}}$  (solid lines, theory) vs. experimental values (points). Subfigures e and f: entropy S as a function of  $\eta$  and  $\lambda$ ; solid lines with markers show experimental estimates, dashed lines their smoothed versions.

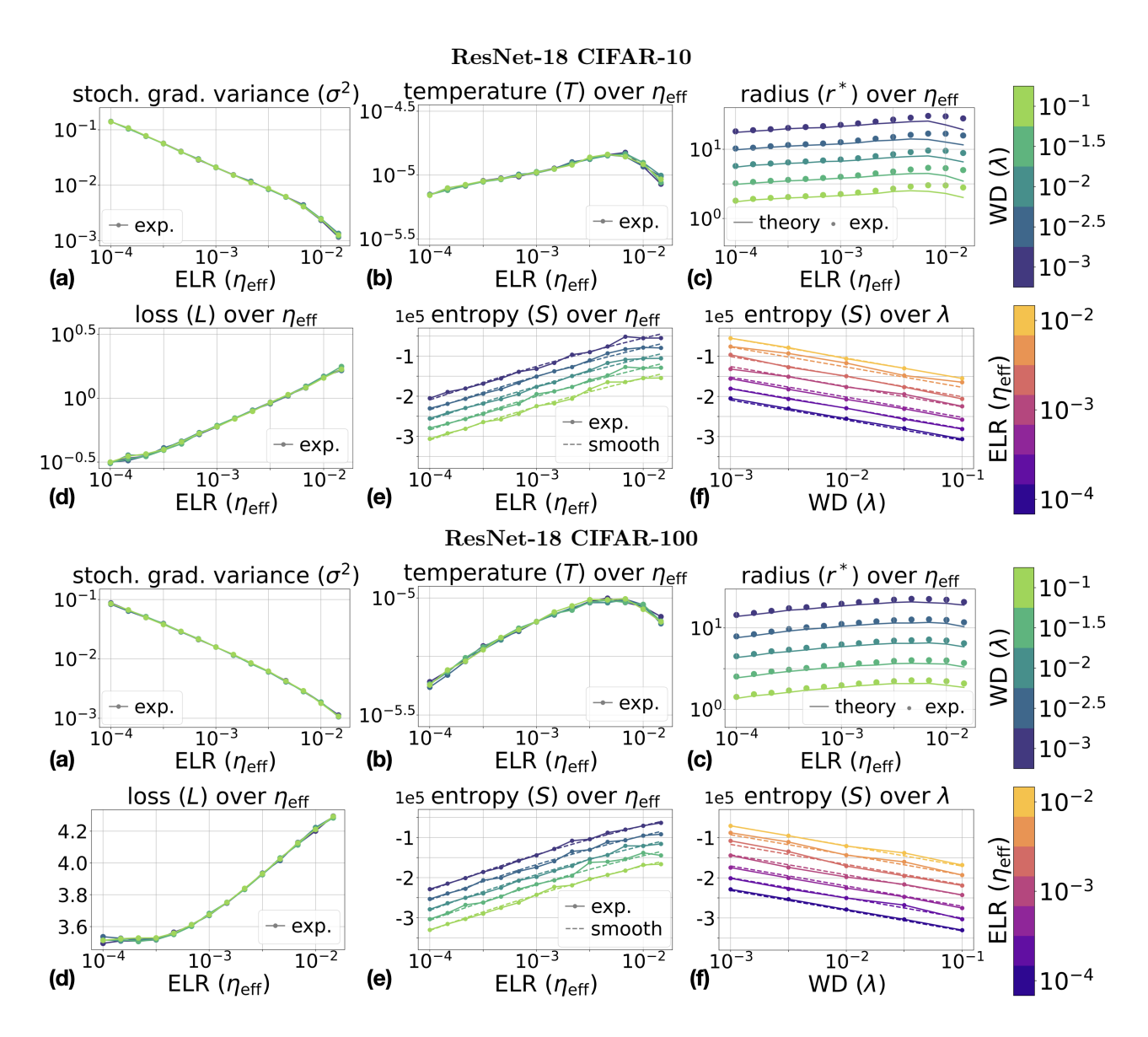


Figure 7: Results for ResNet-18 on CIFAR-10 and CIFAR-100 with fixed ELR  $\eta_{\rm eff}$  and WD  $\lambda$ . Subfigures a, b, d: empirically measured  $\sigma^2$ , mean loss L, and temperature T given by  $T = \frac{\eta_{\rm eff}\sigma^2}{2}$ , respectively. Subfigure c: stationary radius  $r^* = \sqrt{\frac{T(d-1)}{p}}$  (solid lines, theory) vs. experimental values (points). Subfigures d and e: entropy S as a function of  $\eta_{\rm eff}$  and  $\lambda$ ; solid lines with markers show experimental estimates, dashed lines their smoothed versions.

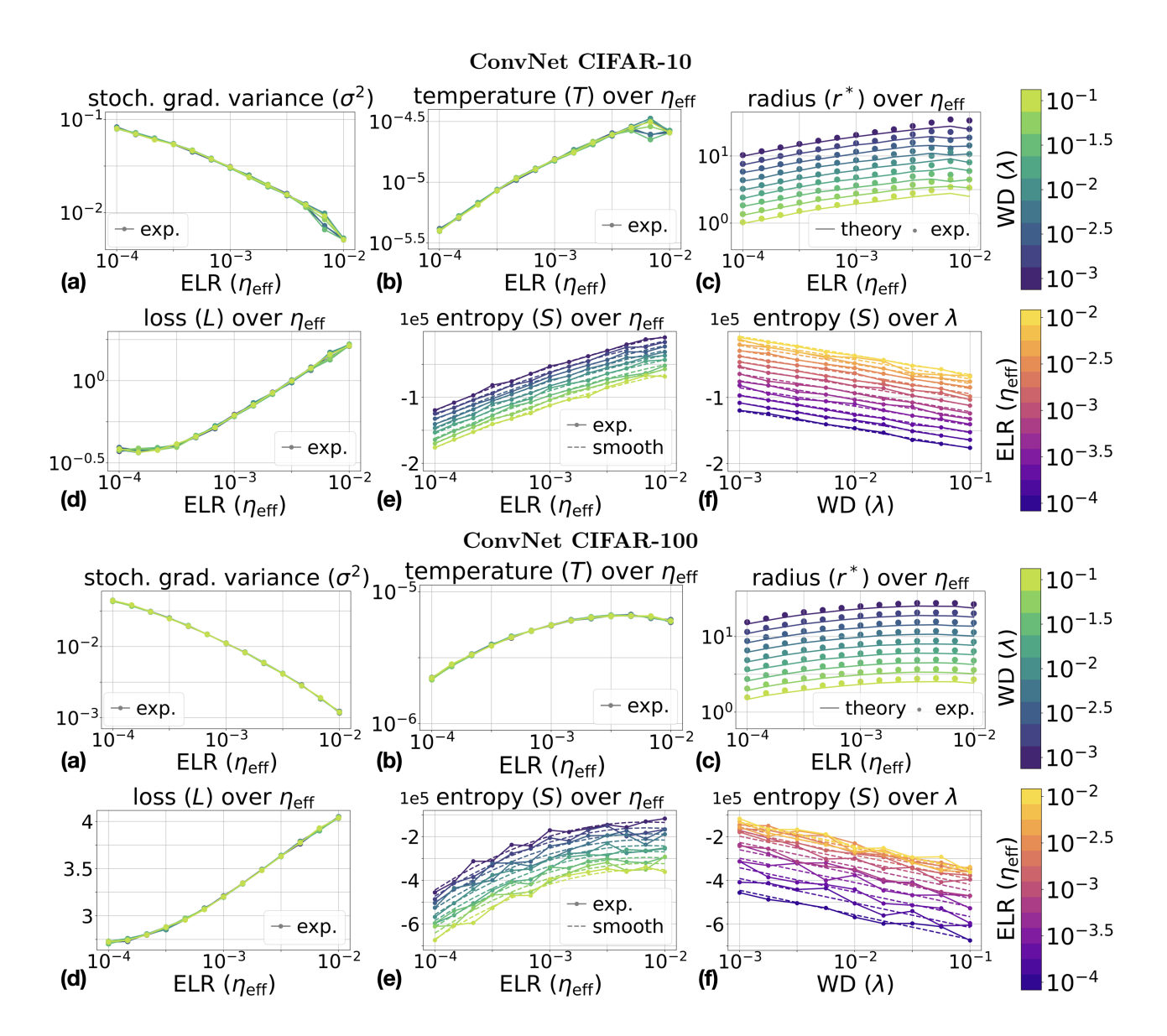


Figure 8: Results for ConvNet on CIFAR-10 and CIFAR-100 with fixed ELR  $\eta_{\rm eff}$  and WD  $\lambda$ . Subfigures a, b, d: empirically measured  $\sigma^2$ , mean loss L, and temperature T given by  $T=\frac{\eta_{\rm eff}\sigma^2}{2}$ , respectively. Subfigure c: stationary radius  $r^*=\sqrt{\frac{T(d-1)}{p}}$  (solid lines, theory) vs. experimental values (points). Subfigures e and f: entropy S as a function of  $\eta_{\rm eff}$  and  $\lambda$ ; solid lines with markers show experimental estimates, dashed lines their smoothed versions.

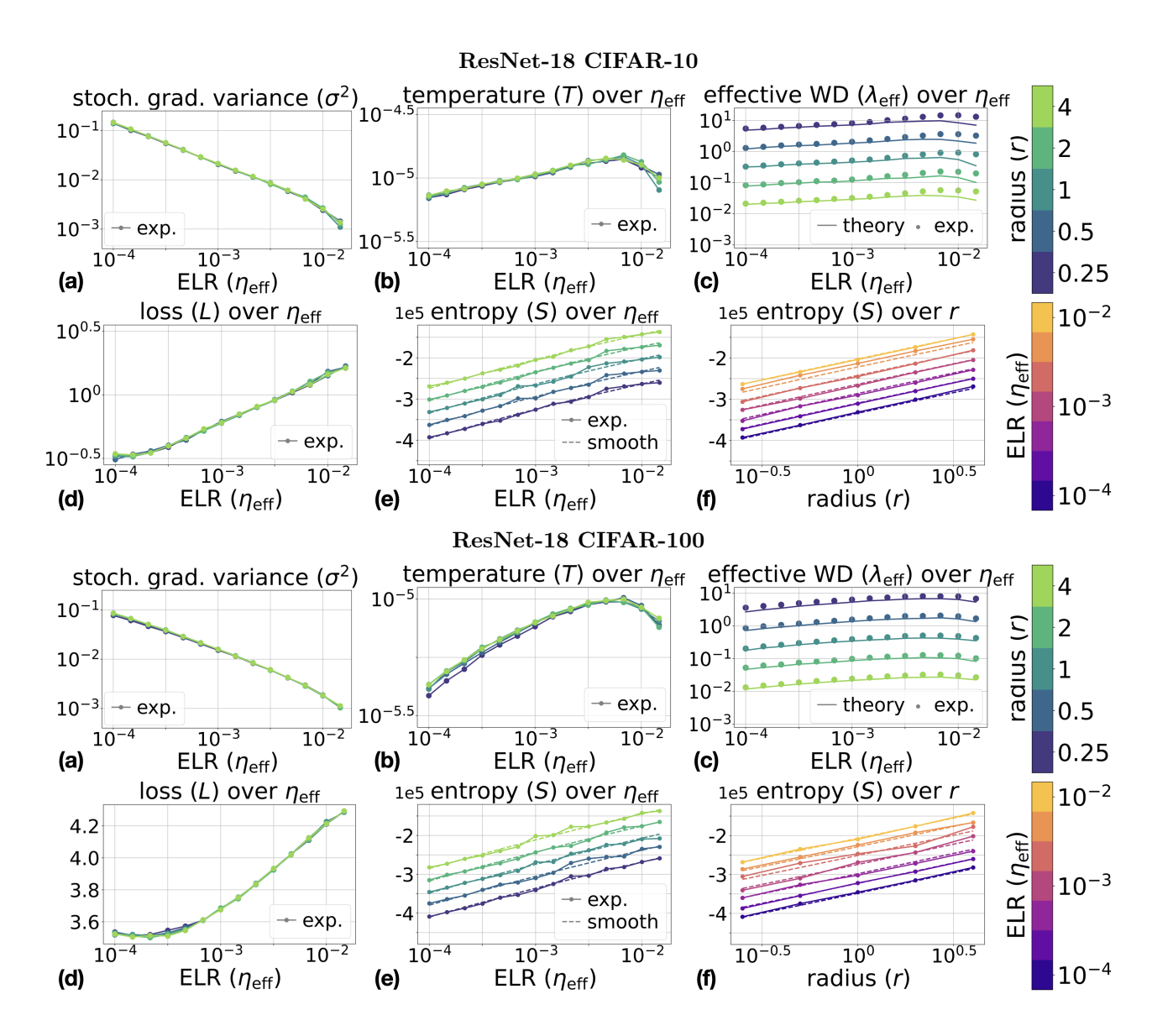


Figure 9: Results for ResNet-18 on CIFAR-10 and CIFAR-100 on a fixed sphere with radius r and fixed ELR  $\eta_{\rm eff}$ . Subfigures a, b, d: empirically measured  $\sigma^2$ , mean loss L, and temperature T given by  $T = \frac{\eta_{\rm eff}\sigma^2}{2}$ , respectively. Subfigure c: effective weight decay coefficient  $\lambda_{\rm eff} = \frac{T(d-1)}{2V}$  for  $V = \frac{r^2}{2}$  (solid lines, theory) vs. experimental values (points). Subfigures e and f: entropy S as a function of  $\eta_{\rm eff}$  and r; solid lines with markers show experimental estimates, dashed lines their smoothed versions.

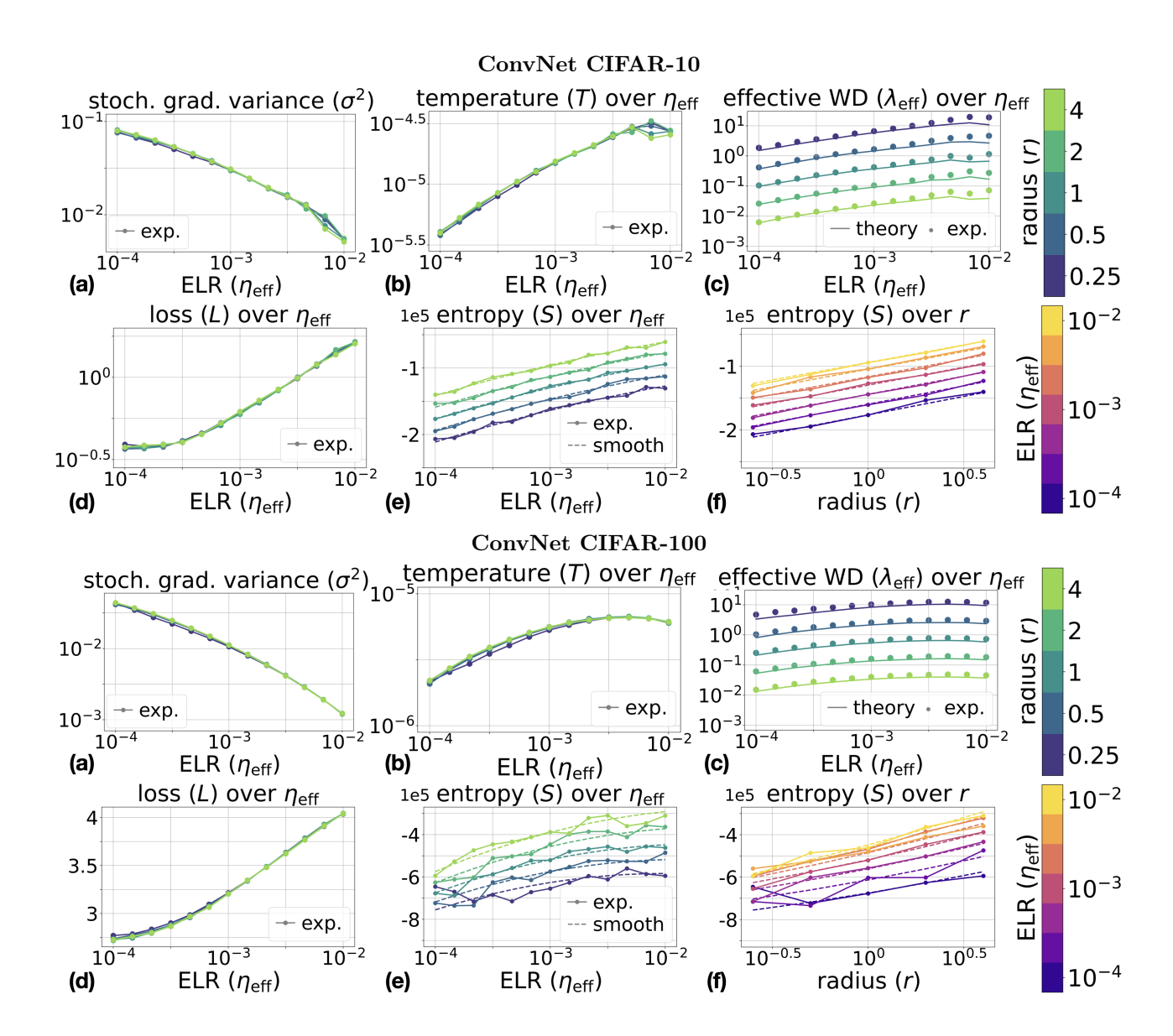


Figure 10: Results for ConvNet on CIFAR-10 and CIFAR-100 on a fixed sphere with radius r and fixed ELR  $\eta_{\rm eff}$ . Subfigures a, b, d: empirically measured  $\sigma^2$ , mean loss L, and temperature T given by  $T = \frac{\eta_{\rm eff}\sigma^2}{2}$ , respectively. Subfigure c: effective weight decay coefficient  $\lambda_{\rm eff} = \frac{T(d-1)}{2V}$  for  $V = \frac{r^2}{2}$  (solid lines, theory) vs. experimental values (points). Subfigures e and f: entropy S as a function of  $\eta_{\rm eff}$  and r; solid lines with markers show experimental estimates, dashed lines their smoothed versions.

#### G DISCRETIZATION ERROR OF SDE

In this section, we discuss the discrepancy between the theoretical and experimental values of the stationary radius  $r^*$ , illustrated in Subfigure 2c.

Correcting SDE predictions Since the SDE framework models continuous-time dynamics, the full-batch gradient  $\nabla L(\boldsymbol{w})$ , which is orthogonal to  $\boldsymbol{w}$ , does not contribute to the centrifugal force and therefore does not influence the radius dynamics. Although stochastic gradients  $\nabla L_{\mathcal{B}_k}(\boldsymbol{w})$  are also orthogonal to  $\boldsymbol{w}$ , the Ito's correction term, arising from the quadratic variation of Brownian motion  $((d\boldsymbol{B}_t)_i^2 = dt)$ , introduces an additional deterministic centrifugal force. Because the SDE formulation only approximates discrete-time training dynamics, discrepancies between the continuous and discrete descriptions grow with larger  $\eta_{\text{eff}}$  (fixed sphere/fixed ELR cases) or larger  $\eta\lambda$  (fixed LR case).

To account for this mismatch, we introduce a geometric correction that explicitly considers both the deterministic and stochastic components of the gradient. A similar geometric reasoning has been discussed in Kosson et al. (2024). Specifically, we focus on the stationary regime, where the centrifugal force (due to stochastic gradients) and the centripetal force (induced by weight decay) are in equilibrium, as illustrated in Figure 11. Since the stochastic gradient  $\nabla L_{\mathcal{B}_k}(\boldsymbol{w}_k)$  is orthogonal to the weight vector  $\boldsymbol{w}_k$  (**P2**), we can apply the Pythagorean theorem to describe their relationship

$$||w_{k+1}||^2 = (1 - \eta \lambda)^2 ||w_k||^2 + \eta^2 ||\nabla L_{\mathcal{B}_k}(\boldsymbol{w}_k)||^2$$
(111)

Taking the expectation of both sides over the stationary distribution, we get  $\mathbb{E}\|\boldsymbol{w}_k\|^2 = \mathbb{E}\|\boldsymbol{w}_{k+1}\|^2 = \mathbb{E}\|\boldsymbol{w}\|^2$  and  $\mathbb{E}\|\nabla L_{\mathcal{B}_k}(\boldsymbol{w}_k)\|^2 = \|\nabla L_{\mathcal{B}}(\boldsymbol{w})\|^2$ . Hence

$$\mathbb{E}\|\boldsymbol{w}\|^2 = \eta^2 \mathbb{E}\|\nabla L_{\mathcal{B}}(\boldsymbol{w})\|^2 + (1 - \eta\lambda)^2 \mathbb{E}\|\boldsymbol{w}\|^2$$
(112)

$$\mathbb{E}\|\boldsymbol{w}\|^2 = \eta^2 \mathbb{E}\|\nabla L_{\mathcal{B}}(\boldsymbol{w})\|^2 + (1 - 2\eta\lambda + \eta^2\lambda^2)\mathbb{E}\|\boldsymbol{w}\|^2$$
(113)

$$\eta \mathbb{E} \|\nabla L_{\mathcal{B}}(\boldsymbol{w})\|^2 = (2\lambda - \eta \lambda^2) \mathbb{E} \|\boldsymbol{w}\|^2$$
 (114)

We further assume that both  $\eta$  and  $\lambda$  are small  $(\eta, \lambda \ll 1)$ , allowing us to neglect the term  $\eta \lambda^2 \mathbb{E} \|\boldsymbol{w}\|^2$  as a higher-order approximation. Additionally, we assume that the variance of  $\|\boldsymbol{w}\|^2$  is negligible, which enables us to write (using **P1**)

$$rac{\eta \lambda \|oldsymbol{w}_k\|}{\eta \|
abla L_{\mathcal{B}_k}(oldsymbol{w}_k)\|}$$

Figure 11: The balance between centrifugal and centripetal forces, which preserves the weight norm  $\|\boldsymbol{w}_k\|$  after the SGD step. Stochastic gradient  $\nabla L_{\mathcal{B}_k}(\boldsymbol{w}_k)$  is orthogonal to the weight vector  $\boldsymbol{w}_k$ .

$$\mathbb{E}\|\nabla L_{\mathcal{B}}(\boldsymbol{w})\|^{2} = \mathbb{E}\left[\frac{\|\nabla L_{\mathcal{B}}(\overline{\boldsymbol{w}})\|^{2}}{\|\boldsymbol{w}\|^{2}}\right] \approx \frac{\mathbb{E}\|\nabla L_{\mathcal{B}}(\overline{\boldsymbol{w}})\|^{2}}{\mathbb{E}\|\boldsymbol{w}\|^{2}}$$
(115)

Therefore, we get the following equation, which ties  $\mathbb{E}\|\boldsymbol{w}\|^2$  and  $\mathbb{E}\|\nabla L_{\mathcal{B}}(\boldsymbol{w})\|^2$ 

$$\eta \frac{\mathbb{E}\|\nabla L_{\mathcal{B}}(\overline{\boldsymbol{w}})\|^2}{\mathbb{E}\|\boldsymbol{w}\|^2} = 2\lambda \,\mathbb{E}\|\boldsymbol{w}\|^2 \tag{116}$$

Finally, we express the expectation of stochastic gradient norm via the covariance matrix trace and the expectation of the full-batch gradient norm (Eq. 3):

$$\mathbb{E}\|\nabla L_{\mathcal{B}}(\overline{\boldsymbol{w}})\|^{2} = \mathbb{E}\|\nabla L(\overline{\boldsymbol{w}}) + (\boldsymbol{\Sigma}_{\overline{\boldsymbol{w}}})^{1/2}\boldsymbol{\varepsilon}\|^{2} = \mathbb{E}\|\nabla L(\overline{\boldsymbol{w}})\|^{2} + 2\mathbb{E}\left[\nabla L(\overline{\boldsymbol{w}})^{T}(\boldsymbol{\Sigma}_{\overline{\boldsymbol{w}}})^{1/2}\boldsymbol{\varepsilon}\right] + \\ + \mathbb{E}\|(\boldsymbol{\Sigma}_{\overline{\boldsymbol{w}}})^{1/2}\boldsymbol{\varepsilon}\|^{2} = \mathbb{E}\|\nabla L(\overline{\boldsymbol{w}})\|^{2} + \operatorname{Tr}\boldsymbol{\Sigma}_{\overline{\boldsymbol{w}}}$$
(117)

Thus, the resulting relation is

$$\eta \frac{\operatorname{Tr} \mathbf{\Sigma}_{\overline{\boldsymbol{w}}} + \mathbb{E} \|\nabla L(\overline{\boldsymbol{w}})\|^2}{\mathbb{E} \|\boldsymbol{w}\|^2} = 2\lambda \, \mathbb{E} \|\boldsymbol{w}\|^2$$
(118)

By denoting  $r_{\text{discr}}^* = \mathbb{E} \| \boldsymbol{w} \| \approx \sqrt{\mathbb{E} \| \boldsymbol{w} \|^2}$ , we can compare this discrete prediction of radius to the continuous-time prediction  $r_{\text{SDE}}^*$ . In the fixed LR case, we have

$$r_{\text{discr}}^* = \sqrt[4]{\frac{\eta}{2\lambda}} (\text{Tr}\, \mathbf{\Sigma}_{\overline{\boldsymbol{w}}} + \mathbb{E} \|\nabla L(\overline{\boldsymbol{w}})\|^2), \qquad r_{\text{SDE}}^* = \sqrt[4]{\frac{\eta\sigma^2(d-1)}{2\lambda}} = \sqrt[4]{\frac{\eta}{2\lambda}} \, \text{Tr}\, \mathbf{\Sigma}_{\overline{\boldsymbol{w}}}$$
 (119)

In the fixed ELR case,  $\eta = \eta_{\text{eff}} \mathbb{E} ||w||^2$ , so the values of  $r^*$  and  $r^*_{\text{SDE}}$  are

$$r_{\text{discr}}^* = \sqrt{\frac{\eta_{\text{eff}}}{2\lambda} \left( \text{Tr} \, \mathbf{\Sigma}_{\overline{\boldsymbol{w}}} + \mathbb{E} \|\nabla L(\overline{\boldsymbol{w}})\|^2 \right)}, \qquad r_{\text{SDE}}^* = \sqrt{\frac{\eta_{\text{eff}}\sigma^2(d-1)}{2\lambda}} = \sqrt{\frac{\eta_{\text{eff}}}{2\lambda}} \, \text{Tr} \, \mathbf{\Sigma}_{\overline{\boldsymbol{w}}}$$
 (120)

In the fixed sphere case, the values of effective WD  $\lambda_{\rm eff,discr}$  and  $\lambda_{\rm eff,SDE}$  are given by

$$\lambda_{\text{eff,discr}} = \frac{\eta_{\text{eff}}}{2r^2} \left( \text{Tr} \, \boldsymbol{\Sigma}_{\overline{\boldsymbol{w}}} + \mathbb{E} \|\nabla L(\overline{\boldsymbol{w}})\|^2 \right), \qquad \lambda_{\text{eff,SDE}} = \frac{\eta_{\text{eff}}}{2r^2} \, \text{Tr} \, \boldsymbol{\Sigma}_{\overline{\boldsymbol{w}}}$$
(121)

We observe that, in all three cases, the expected squared norm of the full-batch gradient is added to the trace of the covariance matrix, thereby correcting the SDE prediction.

**Results** Figure 12 compares the discrete-time and SDE predictions across all four architecture–dataset pairs. We observe that the discrete-time predictions more closely match the experimental results, particularly for larger values of  $\eta$  and  $\eta_{\text{eff}}$ .

#### H OVERPARAMETERIZED MODELS

**Experimental setup** We train a scale-invariant ResNet-18 on the CIFAR-10 dataset. To ensure the model is overparameterized, i.e., capable of fitting the training set with 100% accuracy, we increase the width multiplier to k = 32. The entropy queue size is reduced to 500. Training is performed using several fixed ELR values and a weight decay coefficient of  $\lambda = 10^{-3}$ . All other hyperparameters are identical to those used for the thinner ResNet-18 model trained on CIFAR-10 with k = 4.

Results Figure 13 shows the learning curves for training loss, parameter radius, and gradient-related metrics (the squared norm of the full-batch gradient,  $\|\nabla L(\overline{w})\|^2$ , and the trace of the covariance matrix,  $\operatorname{Tr}\Sigma_{\overline{w}}$ ). We observe that all four metrics stabilize for the three largest ELRs, indicating the onset of stationary behavior. In contrast, for smaller ELRs, the training loss and gradient metrics continue to decrease steadily after approximately  $10^4$  iterations. This behavior closely matches the convergence regime previously reported by Kodryan et al. (2022) or so-called interpolation mode of Ma et al. (2018) and is specific to overparameterized networks.

When overparameterized models enter the interpolation mode (Ma et al., 2018), SGD with a fixed LR behaves similarly to full-batch gradient descent: it converges to a minimum rather than stabilizing at a stationary distribution (Du et al., 2019; Zou et al., 2018; Nacson et al., 2019). This occurs because stochastic fluctuations diminish during training, specifically,  $\text{Tr} \Sigma_{\overline{w}}$  decreases, as shown in Subfigure 13d, so the noise in the stochastic gradients no longer prevents convergence. From a thermodynamic perspective, this corresponds to the limit  $T \to 0$ , where the Gibbs distribution T3 becomes degenerate, concentrating on the microstate i with the lowest energy  $E_i$ .

As optimization approaches the minimum, the centrifugal force  $\eta \nabla L_{\mathcal{B}_k}(\boldsymbol{w}_k)$  weakens due to the decreasing norm of the stochastic gradient. However, the centripetal force,  $-\eta \lambda \boldsymbol{w}_k$ , remains large, gradually driving the radius to shrink. Eventually (after an infinite amount of training iterations) the centripetal force would vanish entirely, and the radius would collapse, leading to fluctuations around the origin, analogous to full-batch gradient descent in the scale-invariant setting Li et al. (2020). Although the radius for small ELRs remains larger than its initial value in Subfigure 13b, it shows a consistent decline after approximately  $10^5$  iterations. In practice, convergence to the loss minimum on the sphere can be slower than convergence to the origin, leading to instabilities and periodic behavior (Lobacheva et al., 2021) caused by an increase in the gradient norm when moving towards the origin.

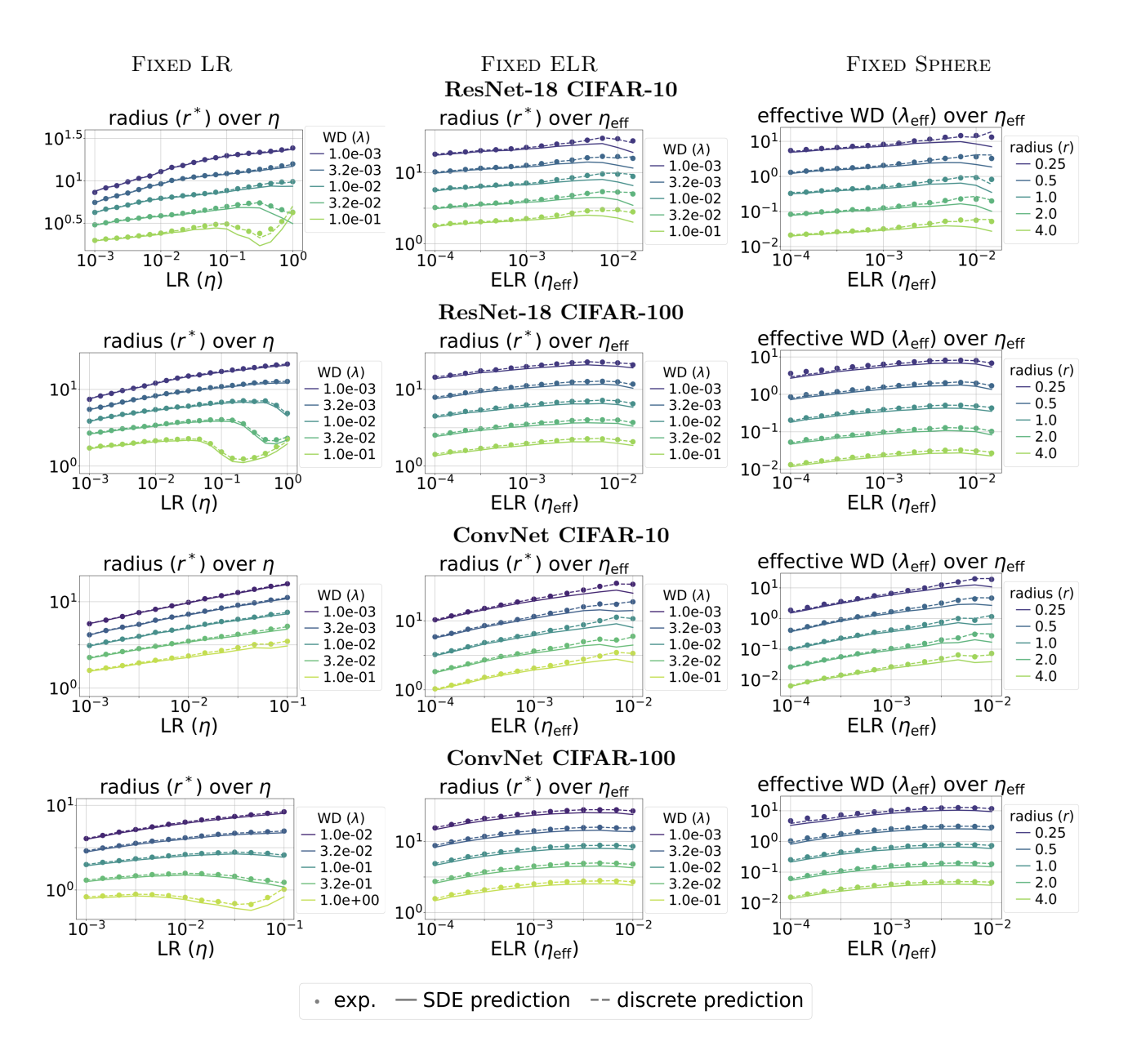


Figure 12: Comparison between the discrete-time and SDE predictions of the stationary radius  $r^*$  for the fixed LR (left column) and fixed ELR (center column) cases, and of the effective weight decay  $\lambda_{\text{eff}}$  for the fixed sphere case (right column).

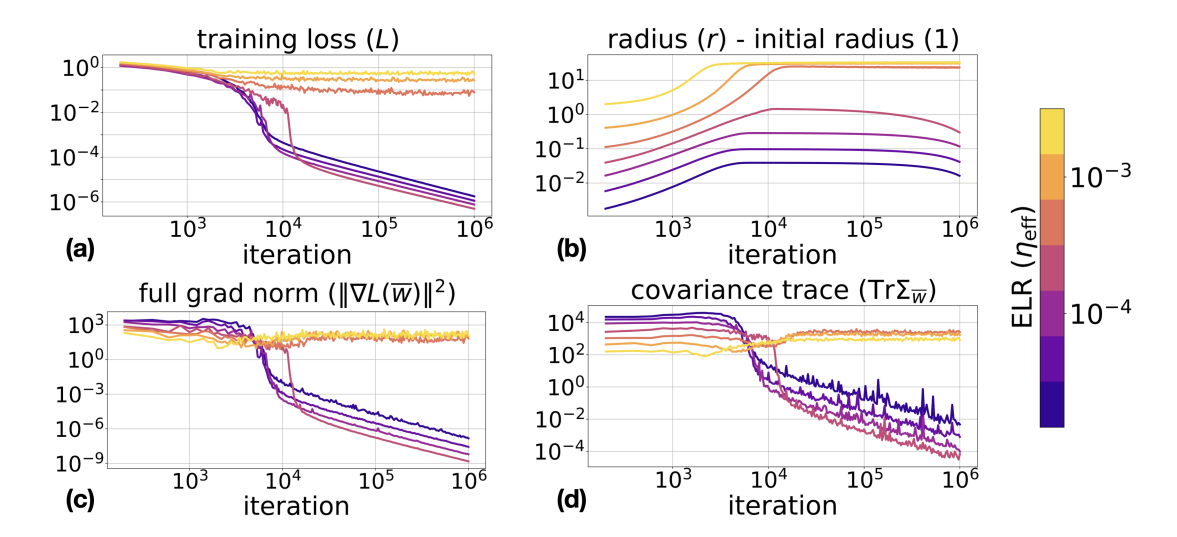


Figure 13: Results for overparameterized ResNet-18 on CIFAR-10 with fixed ELR  $\eta_{\rm eff}$  and weight decay  $\lambda = 10^{-3}$ .